Induced polarization as a tool to characterize permafrost 1. Theory and laboratory experiments

A Revil, J Richard, A Ghorbani, Florence Magnin, P A Duvillard, M Marcer, F Abdulsamad, T Ingeman-Nielsen, Ludovic Ravanel, C Lambiel, et al.

Geophysical Journal International

Geophys. J. Int. (2025) **244,** 1–26
Advance Access publication 2025 November 6
Research Paper

https://doi.org/10.1093/gji/ggaf443

Induced polarization as a tool to characterize permafrost 1. Theory and laboratory experiments

A. Revil,[1] J. Richard,[1,2] A. Ghorbani,[2] F. Magnin,[1] P. A. Duvillard,[2] M. Marcer,[3,4] F. Abdulsamad,[2] T. Ingeman-Nielsen,[3] L. Ravanel,[1] C. Lambiel,[5] X. Bodin,[1] H. Cai,[6,7] X. Hu[6,7] and P. Vaudelet[2]

[1] *Université Savoie Mont—Blanc, CNRS, UMR CNRS* 5204, *EDYTEM, Le Bourget du Lac 73374, France. E-mail: andre.revil@univ-smb.fr*
[2] *NAGA Geophysics, Building C, 229 rue Joseph Fontanet, 73000 Chambéry, France*
[3] *DTU Sustain, Bygning* 115, 2800 *Kgs. Lyngby, Denmark*
[4] *Arctic DTU, Siimuup Aqqutaa* 32, *B*-1280, 3911, *Sisimiut, Greenland*
[5] *Institute of Earth Surface Dynamics, University of Lausanne, CH-1015, Lausanne, Switzerland*
[6] *School of Geophysics and Geomatics, China University of Geosciences and Hubei Subsurface Multi-scale Imaging Key Laboratory, Wuhan* 43074, *China*
[7] *State Key Laboratory of Geological Processes and Mineral Resources, China University of Geosciences, Wuhan* 430074, *China*

Accepted 2025 November 1. Received 2025 September 9; in original form 2025 June 23

SUMMARY

In the last decade, the dynamic Stern layer (DSL) model has proven to be a reliable petrophysical model to comprehend induced polarization data at various scales from the representative elementary volume of a porous rock to the interpretation of field data. Preliminary works have demonstrated that such model can be extended to understand the induced polarization properties of ice-bearing rocks and to interpret field-acquired induced polarization data in the context of permafrost. That being said, the direct effect of ice was let aside. We first review the DSL model in presence of ice and discuss the role of ice as an interfacial protonic dirty semiconductor in the complex conductivity spectra with an emphasis on the role of the complex-valued surface conductivity of ice crystals above 1 Hz. We propose a new combined polarization model including indirect and direct ice effects. By direct effects, we mean the effects associated with changes in the liquid water content and salinity of the pore water. By direct effect, we mean that the role of the interfacial properties of the ice surface and liquid water is still present in the pore space of the porous composite. In this case, the electrical current is not expected to cross the ice crystals. Instead, it would polarize the surface of the ice crystals (and therefore the ice crystals) and generate a very high chargeability that can reach one depending on the value of the volumetric content of ice. We apply the DSL model to a new set of complex conductivity spectra obtained in the frequency range 10 mHz–45 kHz using a collection of 25 rock samples including metamorphic and sedimentary rocks in the temperature range +15/+20 °C to −10/−15 °C. We observe that the model explains very well the observed data in the low-frequency range (10 mHz–1 Hz) without any direct contribution of ice. In the high-frequency range (above 1 Hz), we observe a weak contribution possibly associated with the contribution of ice crystals in low-porosity crystalline rocks. We establish under what conditions the direct contribution of ice can be neglected. We also investigate the role of porosity, cation exchange capacity and freezing curve parameters on the complex conductivity spectra of crystalline and non-crystalline rocks during freezing. Laboratory experiments demonstrate that in most field conditions including permafrost conditions, surface conductivity associated with conduction on the surface of clay minerals (and alumino-silicates in general) is expected to dominate the overall conductivity response. This is in sharp contract with many claims found in the literature. Therefore Archie's law cannot be used as a conductivity equation in this context because of the contribution of surface conductivity. A large experimental and field data set at the Aiguille du Midi (3842 m a.s.l., French Alps)

Intended for publication in Geophysical Journal International, Special issue on Induced Polarization

for the resistivity versus temperature data of granitic rocks demonstrates the role of surface conductivity in the overall conductivity of the rock.

Key words: Electrical properties; Electrical resistivity tomography (ERT); Tomography.

1. INTRODUCTION

The occurrence of gravitational instabilities in Alpine regions has recently increased in response to climate change (*e.g.* Gariano & Guzzetti 2016; Hartmeyer *et al.* 2020; Jacquemart *et al.* 2024). This is especially true for rock falls and landslides associated with the warming of permafrost generally located above 2500 m a.s.l. in the European Alps (*e.g.* Ravanel *et al.* 2010). In turn, this has prompted new research efforts regarding the distribution of permafrost in high-altitude areas and the role of the permafrost warming in the hydromechanical behaviour of ice-bearing rocks and sediments (*e.g.* Magnin *et al.* 2015a; 2015b; Myhra *et al.* 2017; Magnin *et al.* 2017, 2024, b; Cathala *et al.* 2024a). Furthermore, this has also lead to further needs in developing new non-intrusive tools and methods to characterize the properties of porous and fractured bearing-ice materials and monitor their hydromechanical behaviour as a function of temperature (Magnin *et al.* 2015; Herring *et al.* 2023; Offer *et al.* 2025; Chen *et al.* 2025).

Electrical resistivity is broadly used to characterize permafrost since there is a change from a conductive phase (the liquid pore water) to a relatively resistive phase (the ice) (*e.g.* Hauck 2002; Hauck & Vonder Mühll 2003; Hauck *et al.* 2003; Krautblatter *et al.* 2010; Keuschnig *et al.* 2017; Mollaret *et al.* 2019; Scandroglio *et al.* 2021). However, electrical resistivity cannot be considered as a stand-alone technique because it depends on two contributions called hereinafter the bulk and surface conductivities (see Duvillard *et al.* 2018, 2025; Moser *et al.* 2025). Furthermore, in the context of permafrost investigations and analysis, a limitation arises from the fact that the resistivity ranges of other non-icy materials can overlap with that of ice, leading to potential misinterpretations of the field data. This has led some authors to oversimplify the petrophysical models used to interpret electrical resistivity data by keeping only Archie's law (Archie 1942) as a conductivity equation describing the bulk conductivity component of rocks and sediments. Neglecting surface conductivity in low-salinity environments (*e.g.* Herring *et al.* 2019, 2021) is perhaps a questionable assumption because the bulk conductivity contribution is directly proportional to the salinity while the surface conductivity is poorly dependent on the salinity (*e.g.* Waxman & Smits 1968; Duvillard *et al.* 2018). In this paper, we will demonstrate that this assumption is not tenable anymore. Looking at the strength of surface conductivity with respect to the bulk conductivity contribution is the first of our four main goals in this scientific contribution.

Induced polarization is an extension of the electrical resistivity method (e.g. Olhoeft 1981a, b). In addition to measuring the electrical conductivity (the inverse of the resistivity), this non-intrusive geophysical method focuses on the measurements of the quadrature conductivity (frequency-domain) or normalized chargeability (time-domain). These two properties, which are proportional to each other (Revil *et al.* 2017a), characterize the ability of a porous material to reversibly store electrical charges under an applied (imposed) electrical field (Vinegar & Waxman 1984; Titov *et al.* 2002). A rock can be considered as an equivalent circuit with two resistors in parallel to a resistor and a capacitor (e.g. Vinegar & Waxman 1984; Revil 2012, 2013; Fig. 1). One resistor represents the current though the pore space, one resistor represents the conduction through the diffuse layer coating the surface of the grains (frequency independent when the diffuse layers form a continuous path along the material). The last two elements are a resistor in series with a leaking capacitance representing the role of the Stern layer in the conduction/polarization of the grains. Above the freezing temperature and in absence of metallic particles (especially semiconductors such as pyrite and magnetite), this ability is essentially due to the polarization of the electrical double layer (EDL). This EDL (composed by the Stern and diffuse layers, its inner and outer parts, respectively) coats the surface of mineral grains and the grains behave as giant dipoles when submitted to an electrical field or current (Vinegar & Waxman 1984).

Quantitative works using galvanometric induced polarization in the context of permafrost study are scarce (*e.g.* Duvillard *et al.* 2018; Abdulsamad *et al.* 2020; Maierhofer *et al.* 2022; Fereydooni *et al.* 2024, 2025; Moser *et al.* 2025; Limbrock *et al.* 2025). Duvillard *et al.* (2018, 2021) and Abdulsamad *et al.* (2020) developed an induced polarization model based on the dynamic stern layer (DSL) concept. In presence of ice, their model was developed under the assumption that the rock behaves as a closed system (water and especially salts cannot escape the volume under consideration). There are two other goals to this paper. The first is to develop a generalized complex conductivity model to comprehend complex conductivity spectra in a broad range of temperatures including below the freezing temperature. In this paper, we first expand the model of Duvillard *et al.* (2018) by (i) considering open or closed conditions and (ii) we investigate the direct effect of ice on the DSL model in ice-bearing porous rocks and sediments. Indeed, ice itself is a dirty protonic semiconductor. The second goal is to extensively investigate the role of the ice water interface as being responsible for a strong frequency-dependent additional surface conductivity, which can provide ice with an equivalent bulk conductivity that is frequency dependent and a very strong chargeability.

Finally a fourth goal of our paper is to test the predictions of this extended model on a complete database using 25 well-characterized rock sample data to document the value of the exponential freezing curve introduced by Duvillard *et al.* (2018). In doing so, we will neglect the role of the Maxwell–Wagner–Sillars contribution that for unfrozen materials can be seen only at frequencies above 100 Hz to 100 kHz depending on the cation exchange capacity of the material (Fig. 2). A comparison between laboratory data and field data for granite is performed using a data set obtained at the Aiguille du Midi (3842 m a.s.l.) in the French Alps to demonstrate the validity of our petrophysical results when compared to direct field measurements. Further discussions of this model to field data are provided in the second paper of this series for three case studies (Revil *et al.* 2025).

2. THEORETICAL MODEL

2.1. General considerations

We consider a representative elementary volume (REV) of a fractured or porous ice-bearing rock or sediment (Fig. 3). This REV is

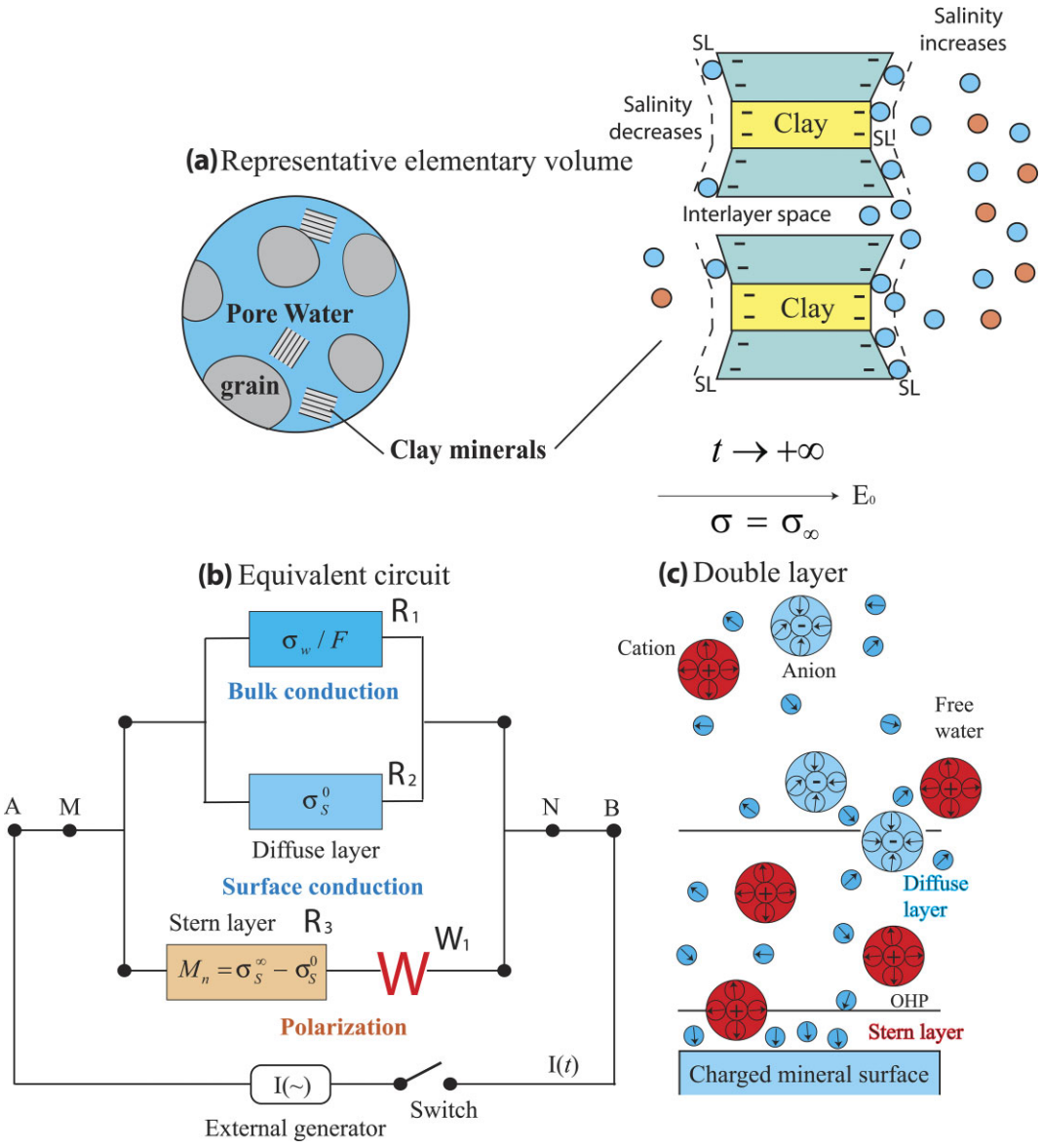

Figure 1. Electrical behaviour of a porous material without ice. **(a)** Representative elementary volume of a rock without ice but in presence of clay minerals. The sketch shows also a fully polarized clay particle under the influence of an external electrical field. F denotes the formation factor, σ_w the pore water conductivity and σ_S^∞ and σ_S^0 the instantaneous and DC (Direct Current) surface conductivity, respectively and M_n the normalized chargeability. (**b**) Equivalent circuit when the diffuse layers of the minerals overlap. The resistances R_1, R_2 and R_3 are associated with the bulk conduction, the diffuse layer conduction and the Stern layer conduction, respectively, while the capacitance W_1 denotes a Warburg (leaking) capacitance associated with the Stern layer polarization. (**c**) Structure of the double layer with the diffuse and Stern layers (OHP stands for the Outer Helmholtz plane).

considered to be homogeneous and isotropic for the sake of simplicity but our model could be easily extended to anisotropic porous rocks considering that the formation factor is a second-order symmetric tensor. We also do not consider here hysteretic effects associated with freezing and thaw, also for the sake of simplicity. The REV can be considered as a closed or open system relative to pore water and salt flow and we discuss below the difference between the two assumptions considering the electrical properties of the material undergoing freezing. This assumption is critical regarding salinity change associated with temperature change below the freezing temperature since the ice itself remains usually salt-free. Finally, we consider electromagnetic fields to be harmonic with a pulsation frequency ω.

With the previous assumptions in mind, the total current density $\mathbf{J}$ (A m^{-2}) entering Ampère's law,

$$\nabla \times \mathbf{H} = \mathbf{J}, \tag{1}$$

($\mathbf{H}$ being the auxiliary magnetic field, expressed in A m^{-1}) is given by,

$$\mathbf{J} = \sigma^* \mathbf{E} + \frac{\partial \mathbf{D}}{\partial t}. \tag{2}$$

Eq. (2) can be seen as a generalized Ohm law (see Vinegar & Waxman 1984). The current density expressed includes the contributions of electromigration, electrodiffusion plus a displacement current density. Usually the contribution of electromigration and

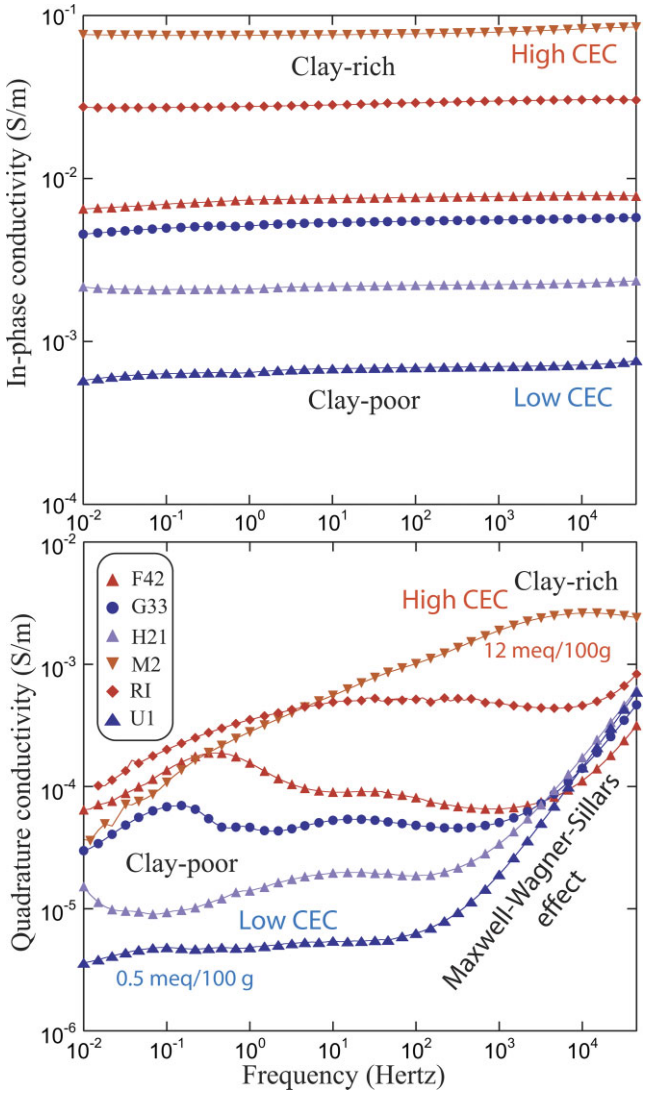

Figure 2. Typical complex conductivity spectra for low- and high-cation exchange capacity (CEC) porous materials. We see that the importance of the Maxwell–Wagner–Sillars contribution depends on the CEC of the material. For smectite-rich materials, we cannot even see it at 45 kHz.

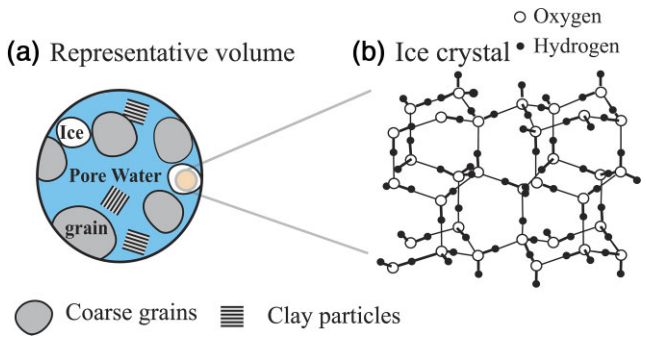

Figure 3. Porous material with ice. (**a**) Representative elementary volume of a rock with ice and clay minerals. (**b**) The ice can be considered as a dirty protonic semiconductor and is susceptible to polarize if the current is forced to go through the crystals. That said the crystals are usually more resistive than the surrounding matrix and the current would flow around them. Another possibility is the polarization of the ice through the charge located on its surface.

electrodiffusion are collected in a complex conductivity term σ^* (Vinegar & Waxman 1984). The displacement field $\mathbf{D}$ itself (in C m^{-2}) is related to the electrical field $\mathbf{E}$ (V m^{-1}) by $\mathbf{D} = \varepsilon * \mathbf{E}$ where $\varepsilon *$ (F m^{-1}) denotes the complex-valued permittivity. In the frequency domain and for harmonic excitations, the expression of the effective (apparent) conductivity $\hat{\sigma}^*$ and effective (apparent) effective (apparent) permittivity $\hat{\varepsilon}^*$ are given as (e.g. Vinegar & Waxman 1984),

$$\nabla \times \mathbf{H} = \hat{\sigma}^* \mathbf{E} \, (= i\omega \hat{\varepsilon}^* \mathbf{E}), \tag{3}$$

where $i^2 = -1$ (i denotes the pure imaginary number). Furthermore, assuming (1) K unique dielectric polarization mechanisms, (2) N unique induced polarization mechanisms (e.g. associated with distinct electrical double layer polarization mechanisms or polarization mechanisms of semiconductors), (3) small conductivity and dielectric increments for each polarization mechanism and (4) that each polarization mechanism can be described by Cole–Cole parametric model at the scale of the REV (Cole & Cole 1941), then we can write the effective (apparent) conductivity and effective (apparent) permittivity as

$$\hat{\sigma}^* = \sigma_\infty - \sum_{n=1}^{N} \frac{\sigma_n^\infty - \sigma_n^0}{1 + (i\omega\tau_n)^{c_n}} + i\omega \left[\varepsilon_\infty + \sum_{k=1}^{K} \frac{\varepsilon_k^0 - \varepsilon_k^\infty}{1 + (i\omega\tau_k)^{c_k}} \right], \tag{4}$$

$$\hat{\varepsilon}^* = \varepsilon_\infty + \sum_{k=1}^{K} \frac{\varepsilon_k^0 - \varepsilon_k^\infty}{1 + (i\omega\tau_k)^{c_k}} - \frac{i}{\omega} \left(\sigma_\infty - \sum_{n=1}^{N} \frac{\sigma_n^\infty - \sigma_n^0}{1 + (i\omega\tau_n)^{c_n}} \right), \tag{5}$$

where the high-frequency conductivity and permittivity are given by,

$$\sigma_\infty = \sum_{n=1}^{N} \sigma_n^\infty, \tag{6}$$

$$\varepsilon_\infty = \sum_{k=1}^{K} \varepsilon_k^\infty. \tag{7}$$

In these equations, τ_k (in s) denotes a relaxation time for the dielectric polarization process labeled k, ε_k^0 and ε_k^∞ denote the low-frequency and high-frequency dielectric constants for the polarization process k ($\Delta\varepsilon_k = \varepsilon_k^0 - \varepsilon_k^\infty$ is called the dielectric increment), and $0 \leq c_k \leq 1$ denotes the Cole–Cole exponent for the dielectric polarization process k, σ_n^0 and σ_n^∞ denotes the low-frequency and high-frequency conductivities associated with the induced polarization contribution n ($\sigma_n^\infty - \sigma_n^0$ is called the normalized chargeability of contribution n or the induced polarizability increment), τ_n denotes the relaxation time for the α-contribution n and $0 \leq c_n \leq 1$ (dimensionless) denotes the Cole–Cole exponent n.

For instance, we can consider simply two polarization processes ($n = 2$) and one dielectric polarization process ($k = 1$). The induced polarization model is associated with the polarization of the electrical double layer coating the clay particles present in the rock plus the effect of the ice acting while the dielectric polarization model is associated with the Maxwell–Wagner–Sillars polarization mechanism associated with the discontinuity of the displacement current at the interface between the different phases of the porous composite including ice (e.g. Revil *et al.* 2015a, b; Misra *et al.* 2016a, b). In the next sections, we describe two of these polarization mechanisms. However, because the ice polarization is characterized by a very high-polarization increment (as demonstrated below) and because ice and the EDL polarization associated with minerals occur more or less in the same frequency domain, we cannot use the superposition principle simply described by eqs (4) and (5). We need to directly combine ice and EDL polarization together by first formulating the problem with ice being a non-polarizing component.

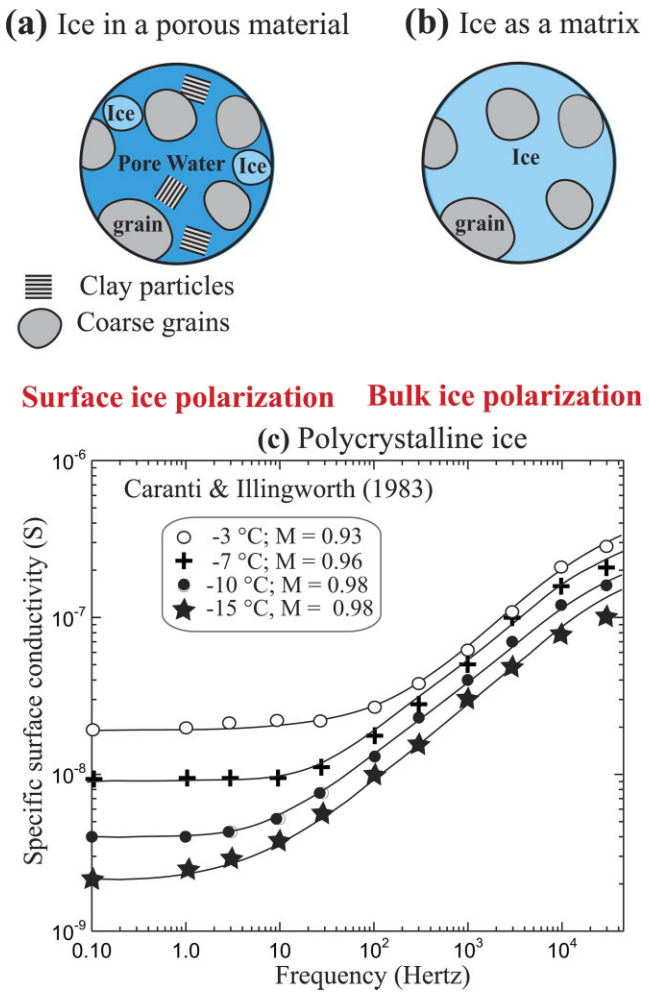

Figure 4. Polarization of the ice. (**a**) In a porous material, ice subdomains are generally embedded into the conductive liquid water. This means that because of their low-electrical conductivity, the electrical current would not penetrate into the ice subdomains to polarize them. The only polarization that may takes place for ice would occur because of their surface charge and associated electrical double layer. (**b**) Ice in a glacier with coarse grains or bounders. In this case, the electrical current lines can flow into the ice and would polarize the ice as a protonic semiconductor. (**c**) Specific surface conductivity (in S) of ice as a function of the frequency and for four different temperatures (experimental data for the specific surface conductance from Caranti & Illingworth 1983). M denotes the chargeability.

2.2. Contribution associated with the double layer in an open system

In this section, we do not consider the direct effect of ice in the polarization of the porous rock. We first assume that the change of water into ice is slow enough so the salinity of the pore water can equilibrate with an infinite reservoir in contact with the porous material so there is no increase in salinity during the transformation of liquid water into ice (open REV). We strongly believe that this assumption hold for permafrost occurring over long timescales. With these assumptions, the complex conductivity of the porous material with inert ice can be written as (Duvillard *et al.* 2018)

$$\sigma^* = \sigma_1^\infty - \frac{M_n^1}{1+(i\omega\tau_1)^{c_1}}, \tag{8}$$

where the instantaneous conductivity σ_1^∞, the DC (Direct Current) conductivity σ_1^0, and the normalized chargeability M_n^1 are given by (see Duvillard *et al.* 2018, for a detailed derivation and Revil 2012, for the fundamental development of the DSL model)

$$\sigma_1^\infty = \theta^m \sigma_w + \theta^{m-1}\rho_g B\,\mathrm{CEC}, \tag{9}$$

$$\sigma_1^0 = \theta^m \sigma_w + \theta^{m-1}\rho_g (B-\lambda)\mathrm{CEC}, \tag{10}$$

$$M_n^1 = \theta^{m-1}\rho_g \lambda\,\mathrm{CEC}, \tag{11}$$

respectively and where σ_w denotes the pore water conductivity (S m^{-1}), ρ_g denotes the mass density of the grains (2700 kg m^{-3} for silico-clastic materials and 2900 kg m^{-3} for carbonates and limestones), θ is the water content (at saturation it is equal to the porosity ϕ), $m >$ (dimensionless) is called the first Archie's exponent of Archie's law, the CEC (C kg^{-1}) denotes the Cation Exchange Capacity of the material and λ and B are two composite mobilities (in m^2 V^{-1} s^{-1}) for polarization and conduction, respectively. The contribution involving the CEC in eqs (9) and (10) corresponds to the surface conductivity while the first contribution corresponds to the bulk conductivity (see Fig. 1). The polarization increment M_n^1 corresponds to the contribution of the Stern layer to the electrical conductivity. When the system is above the freezing temperature ($T \geq T_F$, T denotes the temperature in °C), we assume that the porous material is water-saturated and $\theta = \theta_S = \phi$ (the water content is equal to the water content at saturation θ_S which is equal to the connected porosity ϕ). Below the freezing temperature ($T \leq T_F$), we assume there is a decrease in the liquid water saturation and the water content obeys $\theta \leq \phi$. If the system is open, the salinity will remain the same as long as it has the time to equilibrate with the surrounding reservoir.

2.3. Contribution associated with the double layer in a closed system

If the system is closed, there is an increase in the salinity associated with the formation of ice (assuming the ice is salt-free) when temperature decreases. So, we have (Duvillard *et al.* 2018),

$$\sigma_1^\infty = \theta^{m-1}\left(\sigma_w + B\rho_g \mathrm{CEC}\right), \tag{12}$$

$$\sigma_1^0 = \theta^{m-1}\left[\sigma_w + \rho_g (B-\lambda)\mathrm{CEC}\right], \tag{13}$$

$$M_n^1 = \theta^{m-1}\rho_g \lambda\,\mathrm{CEC}. \tag{14}$$

Our assumption is that this is typically the case of laboratory experiments. We see that directly comparing laboratory and field experiments may be misleading when the bulk conduction mechanism dominates the overall conductivity response of the material. Note however that when surface conductivity dominates the overall conductivity response of the material, the freezing response in closed or open condition is the same. This will be discussed further in the last part of this paper.

The liquid pore water and surface mobilities entering the previous model depend on temperature and if a liquid water/electrolyte is present down to the eutectic temperature (~ -21 to -23 °C), these quantities follow a (classical) linear temperature dependence with T (T is the temperature in °C) (see Duvillard *et al.* 2018, and references therein),

$$\sigma_w(T) = \sigma_w(T_0)\left(1+\alpha_w(T-T_0)\right), \tag{15}$$

$$\lambda(T) = \lambda(T_0)\left(1+\alpha_w(T-T_0)\right), \tag{16}$$

$$B(T) = B(T_0)\left(1+\alpha_w(T-T_0)\right), \tag{17}$$

Table 1. Petrophysical properties of the 25 core samples used in this study. For the CEC, we have 1 cmol kg^{-1} = 1 meq/100 g = 963.20 C kg^{-1}.

Sample	Type	Porosity ϕ (−)	CEC (meq/100 g)	F (−)	σ_S (10^{-4} S m^{-1})
ETAC-01	Micaschist	0.043	1.98	75.6	2.62
ETAC-02	Micaschist	0.012	1.56	303.2	2.50
ETAC-03	Micaschist	0.013	0.56	252.4	3.07
ETAC-04	Micaschist	0.013	1.43	306.1	2.71
ETAC-05	Micaschist	0.038		161.8	7.04
GRO-01	Granite	0.048	1.67	415.7	1.36
GRO-02	Granite	0.046	4.66	97.0	0.99
GRO-21a	Granite	0.018	6.56	127.8	1.21
GRO-21b	Granite	0.037	2.51	93.7	0.50
KAN-02	Granodiorite	0.022	0.68	932.9	0.18
KAN-03a	Granodiorite	0.014	0.36	315.0	0.03
KAN-03b	Granodiorite	0.022	0.47	228.8	0.32
THAB-02	limestone	0.022	3.74	168.8	6.46
THAB-03	marble	0.006	2.538	1067.2	0.27
THAB-04	marble	0.008	0.13	639.5	2.05
THAB-05	marble	0.022	1.01	358.9	3.21
HELB-04	Granite	0.010	2.28	774.8	0.96
LAURI-01	Granite	0.012	1.25	777.9	0.90
MON-01	Paragneiss	0.009	1.30	292.5	2.74
MOURTI-02	Gneiss	0.016	0.47	225.4	3.58
MONET-01	Cargneule	0.420	1.59	7.8	0.01
MONET-02	Marl	0.031	5.63	188.7	5.06
SISI-01	Tonatilite	0.032	4.22	82.8	6.92
SISI-02	Tonatilite	0.015	5.68	493.5	3.97
SISI-03	Tonatilite	0.026	3.01	286.4	1.41

where T_0 denotes the reference temperature ($T_0 = 25$ °C), and $\alpha_w \approx 0.022 \pm 0.003/°C$ denotes the linear temperature coefficient (e.g. Vinegar & Waxman 1984; Revil *et al.* 2017a). The dependence of the mobility of the ionic carriers in the pore liquid water is due to the temperature dependence of the dynamic viscosity of the liquid pore water.

2.4. The freezing curve

The rate of freezing and thaw with temperature depends on the pore size distribution (Luo *et al.* 2024, 2025 and references therein). Therefore, depending on the pore size distribution, liquid water can be present down to a temperature of −23 °C. Duvillard *et al.* (2018) introduced the following simple freezing curve for the water content (see also Coperey *et al.* 2019),

$$\theta(T) = \begin{cases} (\phi - \theta_r) \exp\left(-\frac{T - T_F}{T_C}\right) + \theta_r, & T \leq T_F \\ \phi, & T > T_F \end{cases} \tag{18}$$

where $T_F \leq 0$ °C denotes the macroscopic freezing temperature, $\varphi_m = \phi - \theta_r$ (dimensionless) denotes the maximum volumetric ice content at low temperature, ϕ denotes the porosity (dimensionless), θ_r the residual water content and where the temperature T and the critical temperature T_C are expressed in °C. As explained below, the critical temperature reflects the effect of the pore size distribution on the pregressive freezing of the material when temperature decreases. The ice content at a given temperature is given by $\varphi_i(T) \approx \phi - \theta(T) \leq \varphi_m$, $T \leq T_F$. Eq. (18) is chosen in such a way it provides a fully liquid water saturated material at $T = T_F$ and a residual pore water at low temperatures (around −23 °C) corresponding to pockets of saline water and water films between the ice crystals themselves and the ice crystals and the minerals. The choice of the freezing curve accounts for the pore size-dependent freezing/melting point associated with the curvature of the pores, a phenomenon known as the Gibbs–Thomson effect (Wan *et al.* 2020, and references therein).

During freezing, it is often assumed that ice forms first in the largest pore and when temperature decreases, it forms in smaller and smaller pores growing from inside the pores by keeping a water film at the mineral/ice interface (Anderson *et al.* 2009). This point of view has, however, been recently challenged by recent studies (e.g. Jia *et al.* 2019) that may provide evidence that this may not be always the case. For instance, Nuclear Magnetic Resonance data may suggest that capillary bound water in small pores could be freezing before large pores. *P*-wave testing on frozen rock samples also suggests that a simple ice formation in larger pores cannot explain the measured response (Dou *et al.* 2016). In all cases, however, at a given temperature, there is a salinity variation through the pore space of the porous material that may take some time to equilibrate. During thawing, ice melts first in smaller pores at lower temperatures. When thawing is investigated, the melting temperature of ice T_M is different from the freezing temperature T_F. This effect plays a critical role in hysteretic behaviour of the freeze/thaw (freezing characteristic) curves and the resulting complex conductivity. Because of the stress and strain conditions during freezing, there may be also changes in the pore geometry of soft sediments like soils that may impact in turn the contributions of bulk and surface conduction. As mentioned above, such effects will not be considered in this paper.

2.5. Ice as a semiconductor: should it be considered?

In Sections 2.2 and 2.3, we have assumed that ice is inert with respect to polarization. For crystalline rocks, it does not matter because the total amount of ice remains small but if the porosity of the material is

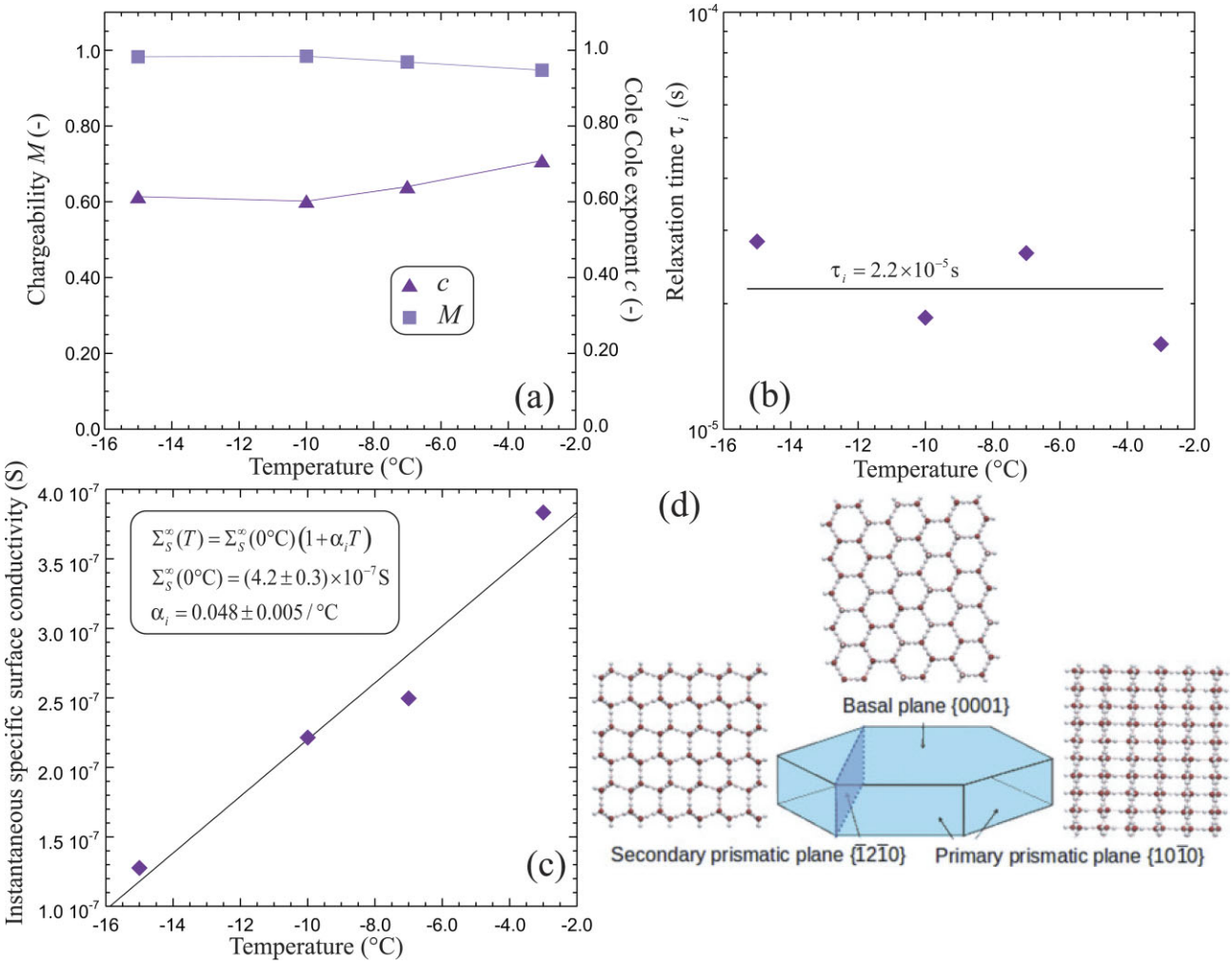

Figure 5. Cole–Cole properties of ice. (**a**) Chargeability and Cole–Cole exponent. (**b**) Instantaneous specific surface conductivity of ice versus temperature. (**c**) Relaxation time versus temperature. (**d**) Ice crystal showing the different crystalline planes hexagonal ice. The surface of the crystal planes is covered by an electrical double layer comprising a Stern layer and a diffuse layer (Daigle 2021). The relaxation time is likely associated with the size of the ice crystals explaining the Debye-type value of the Cole–Cole exponent (above 0.6).

high, the direct polarization effect of ice would be more pronounced. Three questions arise (i) in what frequency range ice is expected to polarize? (ii) What is the effect of the volume fraction of ice in the strength of this polarization? And (iii) what is the mechanism of ice polarization? Is it a bulk or an interfacial polarization mechanism?

It is well-established that ice is a dirty protonic semiconductor with different types of mobile charge carriers including ionic contributions associated in its crystalline framework, holes and protons in the crystalline framework (Eigen & Maeyer 1958). Its surface is also known to conduct electricity (Bullemer & Rielh 1966). According to the literature review made by Kulessa (2007), the electrical conductivity and polarization of ice at a given temperature are controlled by the amount and type of impurities and their distribution in the network of electrically coupled grain boundaries, ice crystal lattices, veins and triple junctions (junctions between three ice crystals, see Auty & Cole 1952; Bullemer & Rielh 1966; Mader 1992; Petrenko & Whitworth 1999).

However, ice remains always a pretty poor electrical conductor and this remains true even at high frequencies (10 kHz). This behaviour is very distinct from other well-studied semiconductors such as pyrite and magnetite (Shuey 1975). As shown in Figs 4(a) and (b), ice can be present in different proportions in the subsurface of the Earth; for the theory developed by Revil *et al.* (2015a, b) for semiconductors to apply, the volume fraction of ice should be both high (therefore at very low temperatures, below −15 °C, in highly porous bodies, porosity >30 per cent) and the conductivity of ice should be greater than the conductivity of the background material. Clearly these conditions are fulfilled only for ice glaciers with a high proportion of ice (Fig. 4b).

In the case sketched in Fig. 4(a), the electrical current lines would not penetrate into the ice crystals because of their high resistivity with respect to the liquid pore water around them. If we consider an equivalent network of resistances, the electrical current would flow in the high-conductive paths as long as there are above a percolation threshold. Therefore only the surface of the ice crystals is expected to polarize through the electrical double layer coating their surface (like for clays). Regarding this EDL, Daigle (2021) demonstrated that 99 per cent of the countercharge in the double layer at the ice/liquid water interface is in the Stern layer. We advocate consequently for a very strong role of the water film at the surface of ice in its polarization in agreement with the seminal paper of Jaccard (1967) and later those of Caranti & Illingworth (1983), Bitelli *et al.* (2004), Kozhevnikov & Antonov (2012) and Kozhevnikov (2022).

Table 2. Petrophysical properties of the 25 core samples used in this study at 20 °C. The normalized chargeability is here computed as the difference between the in-phase conductivity at 10 kHz and 10 mHz.

Sample	σ'(10 mHz) S m^{-1}	σ'(10 kHz) S m^{-1}	M_n S m^{-1}	σ'(3 Hz) S m^{-1}
ETAC-01	3.47e−04	3.87e−04	3.93e−05	2.35e−06
ETAC-02	2.72e−04	3.48e−04	7.58e−05	3.26e−06
ETAC-03	3.28e−04	4.08e−04	7.94e−05	5.88e−06
ETAC-04	2.86e−04	3.30e−04	4.41e−05	2.55e−06
ETAC-05	7.28e−04	8.34e−04	1.06e−04	1.27e−05
GRO-01	1.71e−04	2.11e−04	3.94e−05	2.49e−06
GRO-02	2.83e−04	3.36e−04	5.22e−05	4.79e−06
GRO-21a	3.76e−04	4.86e−04	1.10e−04	1.02e−05
GRO-21b	3.30e−04	4.11e−04	8.06e−05	5.77e−06
KAN-02	1.87e−05	3.07e−05	1.20e−05	2.55e−07
KAN-03a	9.17e−05	1.07e−04	1.50e−05	1.08e−06
KAN-03b	8.98e−05	1.35e−04	4.54e−05	2.24e−06
THAB-02	7.42e−04	8.87e−04	1.45e−04	1.05e−05
THAB-03	3.62e−05	6.95e−05	3.33e−05	2.48e−06
THAB-04	2.19e−04	2.84e−04	6.44e−05	3.24e−06
THAB-05	3.51e−04			6.93e−06
HELB-04	1.43e−04	2.09e−04	6.62e−05	2.49e−06
LAURI-01	1.04e−04	1.41e−04	3.71e−05	1.74e−06
MON-01	2.98e−04	5.88e−04	2.90e−04	2.24e−05
MOURTI-02	4.09e−04	4.58e−04	4.86e−05	4.26e−06
MONET-01	1.33e−03	1.52e−03	1.91e−04	2.09e−05
MONET-02	5.14e−04	5.86e−04	7.22e−05	7.58e−06
SISI-01	7.31e−04	1.13e−03	4.03e−04	5.65e−05
SISI-02	2.98e−04	8.91e−04	5.93e−04	4.96e−05
SISI-03	1.75e−04	2.20e−04	4.50e−05	3.93e−06

Caranti & Illingworth (1983) measured the surface conductivity of ice crystals. This surface conductivity can be characterized by a specific surface conductance or conductivity (in S) $\Sigma_S(\omega)$, which is measurable. The data shown in Fig. 4(c) (from Caranti & Illingworth 1983) indicate that the low-frequency polarization of ice occurs in the frequency range 1–10^5 Hz. The fact that ice polarizes above 1 Hz will be important in what follow. Furthermore, ice crystals can be considered as nearly perfect capacitors with a chargeability close to 1 (Fig. 4c). This high polarizability is mostly due to the frequency dependence of their surface conductivity. Since this data set can be fitted by a Cole–Cole model, we can write the complex specific surface conductivity of ice (in S) as

$$\Sigma_S*(\omega)=\Sigma_i^{\infty}\left(1-\frac{M_i}{1+(i\omega\tau_i)^{c_i}}\right), \tag{19}$$

where Σ_i^{∞} (in S) and M_i (dimensionless) denote the instantaneous specific surface conductivity (which has the dimension of a conductance in S) and chargeability of ice, respectively while τ_i (in s) and c_i (dimensionless) denote the relaxation time and Cole–Cole exponent of ice, respectively. It is likely that the Cole–Cole exponent describes the broadness of the ice crystal size distribution. To give an idea of the Cole–Cole parameters, at −10 °C, we have Σ_i^{∞} $= 2.2 \times 10^{-7}$ S, $M_i = 0.98$, $\tau_i = 1.9 \times 10^{-5}$ s and $c_i = 0.60$ from a fit of the data by Caranti & Illingworth (1983). The low-frequency surface conductance of the surface layer of ice (Ih) Σ_i^0 is on the order of 10^{-9} S, which can be compared to the 10^{-10} S value reported by Jaccard (1967) at −11 °C. The value of the relaxation time is close to the value provided by Petrenko (1993), $\tau_i \approx 5 \times 10^{-5}$ s at −10 °C. Kozhevnikov & Antonov (2012) reported, thanks to time-domain electromagnetic data, a time constant comprised between 5×10^{-5} and 10×10^{-5} s (see also discussion in Kozhevnikov 2022). The very high value of the instantaneous conductivity Σ_i^{∞} (compared to clay minerals for which it is close to 10^{-9} S) implies that the charge carriers on the surface of ice are likely proton, possibly moving through Bjerrum defects on the hydration layer coating the surface of the crystals. Writing $\Sigma_i^{\infty} = \beta(H^+)Q_S$ (where $\beta(H^+)$ is the mobility of the proton on the ice surface and Q_S denotes the surface charge density) and using $\beta(H^+) = 9 \times 10^{-8}$ m^2 s^{-1} V^{-1} (consistent with Petrenko & Maeno 1987, and Table 1 of Stillman *et al.* 2013), we have $Q_S = 2.4$ C m^{-2}, that is, ∼15 elementary charges per nm^2. This implies that the surface of ice is an excellent conductor (high value of Σ_i^{∞}) at the opposite of its bulk component, a point that has been overlooked in the literature in geophysics. Furthermore this implies that most of the charges remain blocked in DC conditions. These protons would remain blocked at the edge of the crystals (in the direction of the electrical field) Since they are locked on the surface of the ice crystals (tangential but no radial movements). The only Direct Current (DC) component remaining is the diffuse layer component, which is very weak in terms of charge density according to Daigle (2021) (most of the countercharge occurs in the Stern layer). In Fig. 5, using the same data set as above, we look at the temperature dependence of the ice properties below the freezing temperature. The relaxation time is temperature independent while the instantaneous surface conductivity varies linearly with temperature.

It follows from the previous arguments that the electrical field has no need to penetrate inside the ice crystals to polarize the bulk volume of ice. It is likely that the specific surface area of the ice crystals play a critical role and since the specific surface area and the volumetric content of ice can be somehow interelated, we use the volumetric ice content as critical state parameter. Note that Maeno & Nishimura (1978) show that ice can have a large range of surface conductivities based on the ice surface conditions. Going a bit further, it means that ice would come into play in the overall polarization process only if its volumetric content is higher than a critical value. For crystalline and low porosity rocks, the ice content would remain low (smaller than the porosity, which is small) and

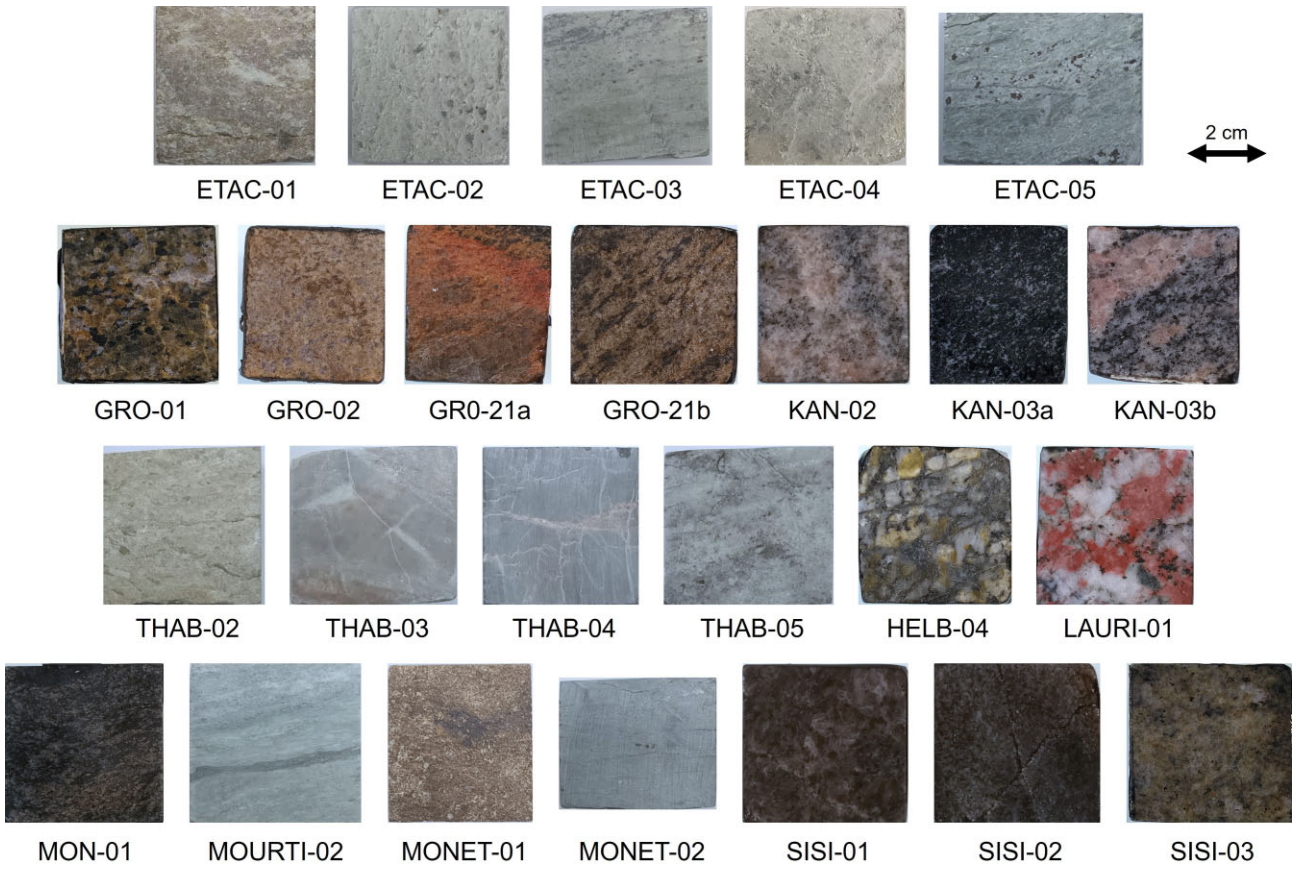

Figure 6. Pictures of the core samples. Most rock samples are crystalline rocks characterized by a rather low porosity (<5 per cent). The samples named ETAC come from Etache close to the Vanoise Park (France), the GR samples are from Greenland, the GRO samples are also from Greenland as well as the KAN samples, the THAB are from the Thabord site (Duvillard *et al.* 2025), the HELB are from the Helbronner in Italian Alpes, LAURI is from the Ecrin Park (France), the MOURTI is from the Valais Alps in Switzerland, the MON (paragneiss) is from Mont-Fort (Switzerland), the MONET samples are from Monetier (MONET-01 is a cargneule from the dolomitic Triassic formation), and finally the SISI samples are from Greenland. The properties of the core samples are reported in Tables 1 to 4.

the direct effect of ice as a capacitor would be difficult to observe. So the first conclusion we can draw is that the direct effect of ice is difficult to observe in crystalline rocks.

We can go one step further in our modeling effort. A relatively insulating crystal with a frequency-dependent surface conductivity $\Sigma_S*(\omega)$ can be assimilated to a crystal with an equivalent bulk conductivity $\sim \Sigma_S*(\omega)/d$ where d is the crystal size (e.g. Revil & Glover 1997). Using eq. (19) with a proper renormalization of the specific surface conductivity to a bulk equivalent conductivity, we can write the conductivity of ice as

$$\sigma_i^* = \sigma_i^\infty \left(1 - \frac{M_i}{1+(i\omega\tau_i)^{c_i}}\right), \tag{20}$$

$$\sigma_i^* \approx \sigma_i^\infty \left(\frac{(i\omega\tau_i)^{c_i}}{1+(i\omega\tau_i)^{c_i}}\right), \tag{21}$$

since the chargeability of ice is close to 1. In order to have an idea of the instantaneous conductivity σ_i^∞, we can look at the equivalent conductivity of ice at high frequencies (here ~10 kHz). The literature provides values around 2×10^{-5} S m^{-1} (50 000 Ohm m). The instantaneous conductivity of ice can be written as,

$$\sigma_i^\infty = \rho_i B_i \, \mathrm{CEC}_i, \tag{22}$$

where ρ_i, B_i and CEC_i denote the mass density of ice (kg m^{-3}), the mobility of the protons (m^2 s^{-1} V^{-1}), and the Cation Exchange Capacity of ice (C kg^{-1}). In order to compute the CEC of ice, we need to know the size of the crystals, which is in turn known to be related to the kinetics of freezing. Fast freezing favours ice crystals in the form of needle-like rods with sizes in the range 0.5–100 μm (e.g. Hou *et al.* 2021). Slow freezing favours ice crystals in the form of block-like particles with sizes >100 μm. Taking a crystal size of 1 μm and a surface charge density of 15 elementary charges per nm^2 (2.4 C m^{-2}), we get a CEC_i equal to ~10 meq/100 g, so a value comparable to kaolinite. This is not an exceptionally high value compared to clay minerals.

2.6. A generalized complex conductivity model

Since ice is nucleating and growing in the pore space of the porous material and following the previous statements and observations, we propose to add the ice polarization to the EDL polarization occurring in the pore space of the rock/sediment. Combining eqs (8) and (20), the following complex conductivity for a rock undergoing freezing is obtained

$$\sigma^* = \left[\sigma_1^\infty + \varphi_i \sigma_i^*\right]\left(1 - \frac{M_1}{1+(i\omega\tau_1)^{c_1}}\right), \tag{23}$$

where $M_1 = M_n^1/\sigma_1^\infty$. We assume that the direct contribution of ice to polarization of the rock mixture can be added (through its volumetric portion) to the high-frequency conductivity of the rock.

Table 3. Petrophysical properties of the 25 core samples used in this study. Parameters relevant of the in-phase conductivity versus temperature. The experiments are performed at the pore water conductivity σ_w reported in the second column at $T_0 = 25\ ^\circ$C (the temperature dependence of the liquid pore water conductivity is given in the main text).

Sample	σ_w(25 °C, S m^{-1})	$\sigma'(T_0)$(10^{-4} S m^{-1})	α_T(°C^{-1})	T_F(°C)	T_C(°C)	θ_r(−)
ETAC-01	0.007	4.22	0.021	−2	−1.02	0.0029
ETAC-02	0.010	4.03	0.019	−6	−0.75	0.0006
ETAC-03	0.010	4.74	0.021	−6	−0.83	0.0013
ETAC-04	0.010	5.01	0.019	−2	−1.92	0.0010
ETAC-05	0.007	11.0	0.020	−2	−2.40	0.0020
GRO-01	0.018	1.69	0.021	−3	−0.75	0.0037
GRO-02	0.019	3.35	0.021	−3	−1.10	0.0193
GRO-21a	0.042	3.93	0.021	−2	−0.38	0.0095
GRO-21b	0.042	2.92	0.022	−4	−0.66	0.0150
KAN-02	0.009	0.25	0.021	−5	−0.71	0.0004
KAN-03a	0.038	0.89	0.019	−4	−0.99	0.0009
KAN-03b	0.038	0.92	0.020	−4	−0.75	0.0009
THAB-02	0.015	8.17	0.021	−2	−1.90	0.0020
THAB-03	0.015	0.32	0.019	−4	−1.20	0.0030
THAB-04	0.017	2.10	0.022	−4	−1.00	0.0040
THAB-05	0.017	4.05	0.023	−2	−0.13	0.0020
HELB-04	0.013	1.21	0.024	−2	−1.80	0.0030
LAURI-01	0.016	0.71	0.022	−2	−1.50	0.0030
MON-01	0.020	4.00	0.021	0	−1.65	0.0022
MOURTI-02	0.018	4.20	0.020	−3	−1.05	0.0068
MONET-01	0.012	21.6	0.021	−2	−0.51	0.0060
MONET-02	0.012	5.98	0.021	−2	−1.43	0.0088
SISI-01	0.010	10.7	0.025	−3	−0.40	0.0130
SISI-02	0.010	4.90	0.024	−3	−0.60	0.0100
SISI-03	0.012	2.01	0.021	−3	−0.85	0.0036

Reworking the ice contribution, we obtain:

$$\sigma^* = \left[\sigma_1^\infty + \varphi_i \sigma_i^\infty \left(\frac{(i\omega\tau_i)^{c_i}}{1+(i\omega\tau_i)^{c_i}}\right)\right]\left(1 - \frac{M_1}{1+(i\omega\tau_1)^{c_1}}\right). \quad (24)$$

The instantaneous conductivity of the mixture is obtained as,

$$\sigma_\infty = \sigma_1^\infty + \varphi_i \sigma_i^\infty, \quad (25)$$

$$\sigma_\infty = \theta^m \sigma_w + \theta^{m-1} \rho_g\, B\mathrm{CEC} + \varphi_i \rho_i\, B_i \mathrm{CEC}_i, \quad (26)$$

while the DC (Direct Curent) conductivity σ_0 remains unchanged because of the very small contribution of the DC conductivity of ice below 1 Hz. This yields:

$$\sigma_0 \approx \theta^m \sigma_w + \theta^{m-1} \rho_g (B - \lambda)\mathrm{CEC}; \quad (27)$$

This is the second conclusion obtained in this section. Below approximately 1 Hz, the DSL model developed in Duvillard *et al.* (2018) remains valid. Above this frequency, an additional contribution would show up: the direct contribution of ice.

The chargeability is defined by,

$$M \equiv \frac{\sigma_\infty - \sigma_0}{\sigma_\infty}. \quad (28)$$

Therefore using eq. (24) in the low- and high-frequency ranges, we obtain after few algebraic manipulations, the following expression of the chargeability of the mixture:

$$M \approx \frac{\theta^{m-1}\rho_g \lambda \mathrm{CEC} + \rho_i B_i\, (\phi - \theta)\mathrm{CEC}_i}{\theta^m \sigma_w + \theta^{m-1}\rho_g\, B\mathrm{CEC} + (\phi - \theta)\rho_i\, B_i \mathrm{CEC}_i}. \quad (29)$$

At low ice contents ($\phi - \theta << 1$) and with the surface conductivity associated with clay dominates the conductivity response, we have $M \approx R \equiv \lambda / B = 0.10 \pm 0.02$ as discussed in Duvillard *et al.* (2018) (the dimensionless number R introduced by Revil and coworkers is independent on temperature and saturation, see Revil *et al.* 2017a, note that for kaolinite $R = 0.20$, Piolat *et al.* 2025a). At high-ice contents, the chargeability is proportional to the ice content and at very high-ice contents, we have $M \approx 1$, a point that we will investigate further in the second paper of this series in which we will show that this conclusion is consistent with both field and laboratory data. Similar conclusion could be drawn by using the Percentage Frequency Effect (sometimes called the Resistivity Frequency Effect), which is proportional to the chargeability (Revil *et al.* 2017a).

2.7. Maxwell–Wagner–Sillars contribution

At the interface between water and ice, which have different conductivities and permittivities, Maxwel–Wagner–Sillars polarization (e.g. Sillars 1937; Cosenza *et al.* 2008) is likely to occur and exist even at low frequencies. A process, however, can exist at low frequencies and being mask at these low frequencies by the induced polarization mechanisms described above. This is particularly well-shown by Fig. 2, see Casotti et al. 2025a, showing that when the CEC of the material increases, the critical frequency at which the Maxwell–Wagner–Sillars polarization starts to be visible increases at increasingly higher frequencies (>10 Hertz to 1 kHz, sometimes above 10 kHz depending on the cation exchange capacity of the material (Revil 2012, 2013). We can just consider that there is a high-frequency polarization that can be modelled by a Debye or a Cole–Cole model in order to retrieve the true induced polarization response of the material and that ice may have a strong effect on the Maxwell–Wagner–Sillars polarization of the mixture (see Zorin & Ageev 2017). In order to see the effect of icing on the high-frequency response, we will plot the quadrature conductivity of the rock or sediment at 1 kHz as a function of the temperature. Since at this frequency, the complex conductivity response

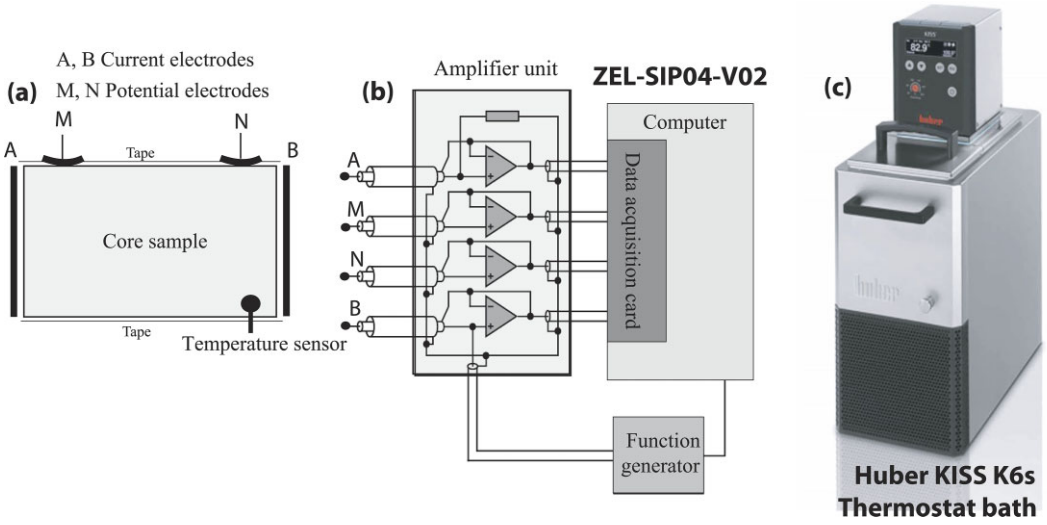

Figure 7. Impedance meter, temperature-controlled bath, and sample holder used for the measurements. (**a**) Position of the electrodes around the core samples. (**b**) ZEL-SIP04-V02 Impedance meter (Zimmermann *et al.* 2008). (**c**) Thermostat bath KISS K6 using a mixture of glycol and water in which the sample holder is located in a plastic bag immersed in a fluid make of a mixture of water and glycol. These equipments (thermal bath and impedance meter) are used to measure the complex conductivity spectra in a broad temperature range (typically +15 °C to −15 °C) and frequency range (10 mHz to 45 kHz).

of the rock is dominated by dielectric effects associated with the Maxwel–Wagner–Sillars polarization, we shall see no temperature dependence above the freezing temperature and a temperature dependence below the freezing temperature associated with the replacement of the liquid water (high-frequency relative permittivity around 80) by ice (high-frequency relative permittivity around 3.2).

2.8. Summary of the model predictions

The model leads to five predictions that can be checked with experimental data.

(1) Surface conductivity dominates bulk conductivity. This is true above freezing conditions for low-salinity pore waters, this remains true below freezing conditions in Alpine areas. Therefore Archie's should not be used as a conductivity equation but remains valid as a relationship between the formation factor and the porosity. By surface conductivity, we mean the conductivity mostly associated with the CEC of the alumino-silicates above and below the freezing conditions. Note that below the freezing temperature, the presence of ice would further enhance surface conductivity.

(2) Normalized conductivity and surface conductivity are proportional to each other. This observation is truly crucial because it offers a way to use induced polarization to infer surface conductivity in field conditions. We will check if it is still true below the freezing temperature.

(3) Below 1 Hz, the conductivity and the normalized chargeability follows the same dependence with the temperature, which can be described by an exponential freezing curve. This prediction implies that we may use, in the future, induced polarization as a geothermometer exactly the way induced polarization is used as a geothermometer in hydrothermal systems (see Piolat *et al.* 2025b) but for different reasons.

(4) For crystalline rocks, the direct polarization effects associated with ice is expected to be difficult to observe because of the very small volume fraction of ice with respect to the total volume of ice. Indeed, the direct contribution of ice depends on the ice content. The ice content cannot be higher than the porosity, which is low. For highly porous rocks, the situation would be very different (for instance for rock glaciers as discussed in the companion paper).

(5) At 1 kHz, if the Maxwel–Wagner–Sillars polarization dominates the overall polarization response of a rock or a sediment, the associated quadrature conductivity is independent of the temperature above the freezing temperature. The quadrature conductivity depends on saturation of the liquid water phase below the freezing temperature. As shown in Fig. 2, the Maxwel–Wagner–Sillars polarization may exist at much lower frequencies but would not show up because of the induced polarization contribution, which depends on the CEC of the material.

3. EXPERIMENTS

3.1. Development of an experimental database

We consider 25 core samples (Fig. 6) including 22 crystalline rock and 3 sedimentary rocks (see Tables 1–4). The samples labelled ETAC come from Etache close to the Vanoise Park (France, see Cathala *et al.* 2024a). The samples labelled GR, SISI, GRO and KAN are all from Greenland (Marcer *et al.* 2024; Marcer *et al.* 2025). The THAB samples are from the Thabord site (Duvillard *et al.* 2025). The HELB are from the Helbronner in Italian Alps. The LAURI sample is from the Ecrin Park (France). The MOURTI sample is from Switzerland. More precisely the Pointes de Mourti correspond to a mountain range in the Swiss Pennine Alps in the Canton of Valais. The MON sample is from Mont-fort (Switzerland, paragness) while the MONET samples are from Monetier (MONET-01 is a cargneule from the dolomitic Triassic formation, Cathala *et al.* 2024b). The samples are chosen to help the interpretation of field data at various test sites where the acquisition of field data were performed (see the second paper of this series). The samples are first dried during 24 hr at about 50 °C and then saturated under vacuum with a very low pore water conductivity corresponding to snow melt (the snow was collected at Val Thorens, its snow melt conductivity at 25 °C is 10 μS cm^{-1}). This snowmelt is representative of the infiltrating water in most field conditions met in Alpine environments. The samples were left in the solution at least

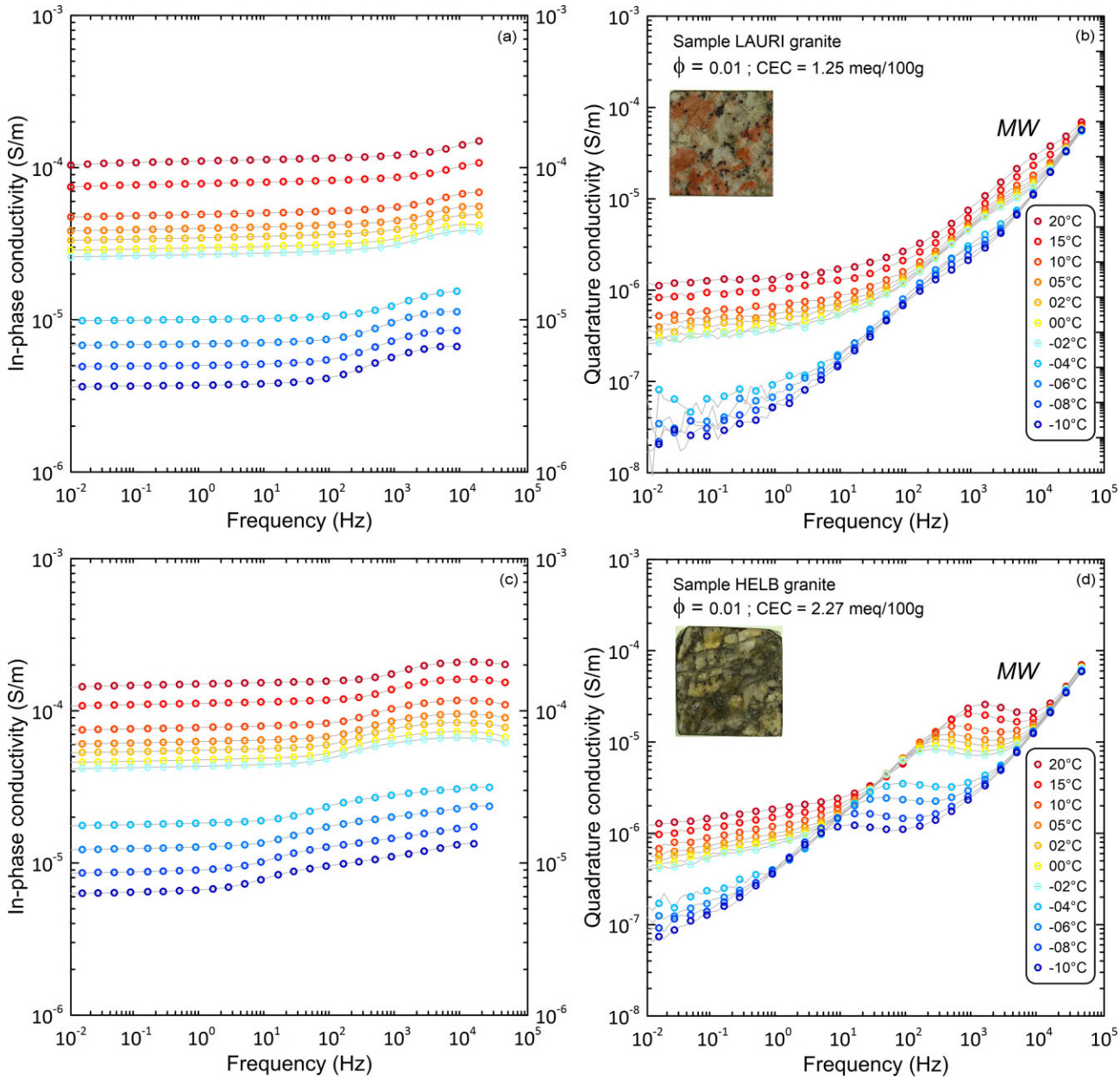

Figure 8. Complex conductivity spectra. (**a**) In-phase conductivity of Sample LAURI (granite). (**b**) Quadrature conductivity of Sample LAURI (granite). (**c**) In-phase conductivity of Sample ELB (granite). (**d**) Quadrature conductivity of Sample HELB (granite). MW stands for Maxwell–Wagner–Sillars polarization. The lines are just guides for the eyes.

1 month until their pore water conductivity stabilizes, which was checked by measuring their conductivity over time until asymptotic conditions were reached. The pore water conductivity at equilibrium with the minerals is higher than the initial pore water conductivity and typically at 0.017 ± 0.002 S m^{-1} at 25 °C, i.e. 170 ± 20 μS cm^{-1} at 25 °C, so one order of magnitude higher than the snowmelt water conductivity). This conductivity is the final conductivity of the bucket in which the samples are stored after saturation the vacuum chamber with the degassed snowmelt solution.

The complex conductivity measurements are performed with the high-precision ZEL-SIP04-V02 impedance meter (see Fig. 7 and Zimmermann *et al.* 2008). The complex conductivity spectra are obtained in the frequency range between 10 mHz to 45 kHz by measuring the amplitude and phase of the impedance. We use four self-adhesive carbon electrodes to perform the measurements (Fig. 7).

The measured impedance is converted into complex conductivity using the geometric factor calculated based on the geometry of the sample and the position of the ABMN electrodes (AB denote the current electrodes and MN the voltage electrodes). The surface area of the electrodes is accounted for in the numerical calculations. The samples are put in a plastic impermeable bag and immersed into a thermally controlled bath (Kiss K6 from Huber; see Fig. 7) with a solution of monoethylene glycol mixed with water. The temperature of the bath is regulated by a precision of 0.1 °C and controlled by an independent thermometer. We investigated the complex conductivity measurement over the range of + 20 °C to −15 °C.

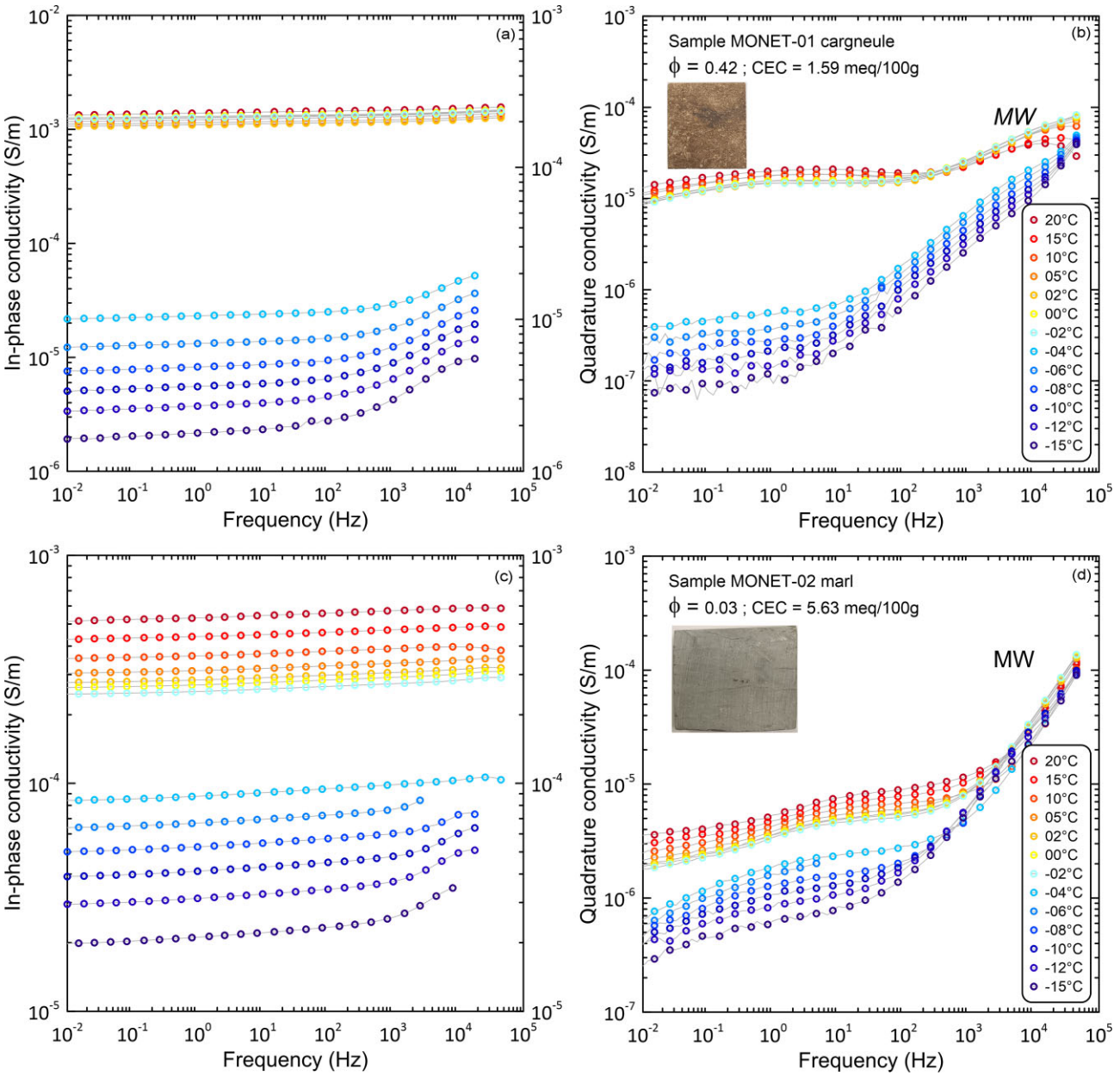

Figure 9. Complex conductivity spectra. (**a**) In-phase conductivity of Sample MONET-01 (cargneule issued from dolomitic Triassic formations). (**b**) Quadrature conductivity of Sample MONET-01 (cargneule). (**c**) In-phase conductivity of Sample MONET-02 (marl). (**d**) Quadrature conductivity of Sample MONET-02 (marl). MW stands for Maxwell–Wagner–Sillars polarization. The lines are just guides for the eyes.

In order to characterize the rock samples, we perform two additional petrophysical measurements, the porosity and the CEC. The CEC is determined using the cobalt hexamine chloride method (Aran *et al.* 2008), which is a titration method of the surface active sites of the mineral surface. Because clay minerals have a high-specific surface areas, their CEC dominates the overall CEC response of porous rocks. The porosity data are obtained using the volume of the samples and their dry and water-saturated weights. The values of the CEC and porosity data are reported in Table 1. As expected, the porosity of most of the rock samples is very low (<4 per cent) and their CEC is comprised between 0.3 and 7 meq/100 g with 1 cmol kg^{-1} = 1 meq/100 g = 963.20 C kg^{-1}.

3.2. Complex conductivity spectra

Figs 8–10 display some representative complex conductivity spectra of six samples. We display the in phase and quadrature conductivity spectra. The in-phase conductivity characterizes the ability of the rock to conductivity an electrical current and the quadrature conductivity its ability to reversibly store electrical charges. Fig. 8(d) (HELB granite) is a very good example why the electrical properties should be evaluated over the frequency spectrum rather than evaluated at a single frequency. This is due to the shift of the relaxation peaks with the temperature itself. All the samples show a significant decrease in the conductivity and quadrature conductivity with the temperature with a characterized drop below the freezing tempera-

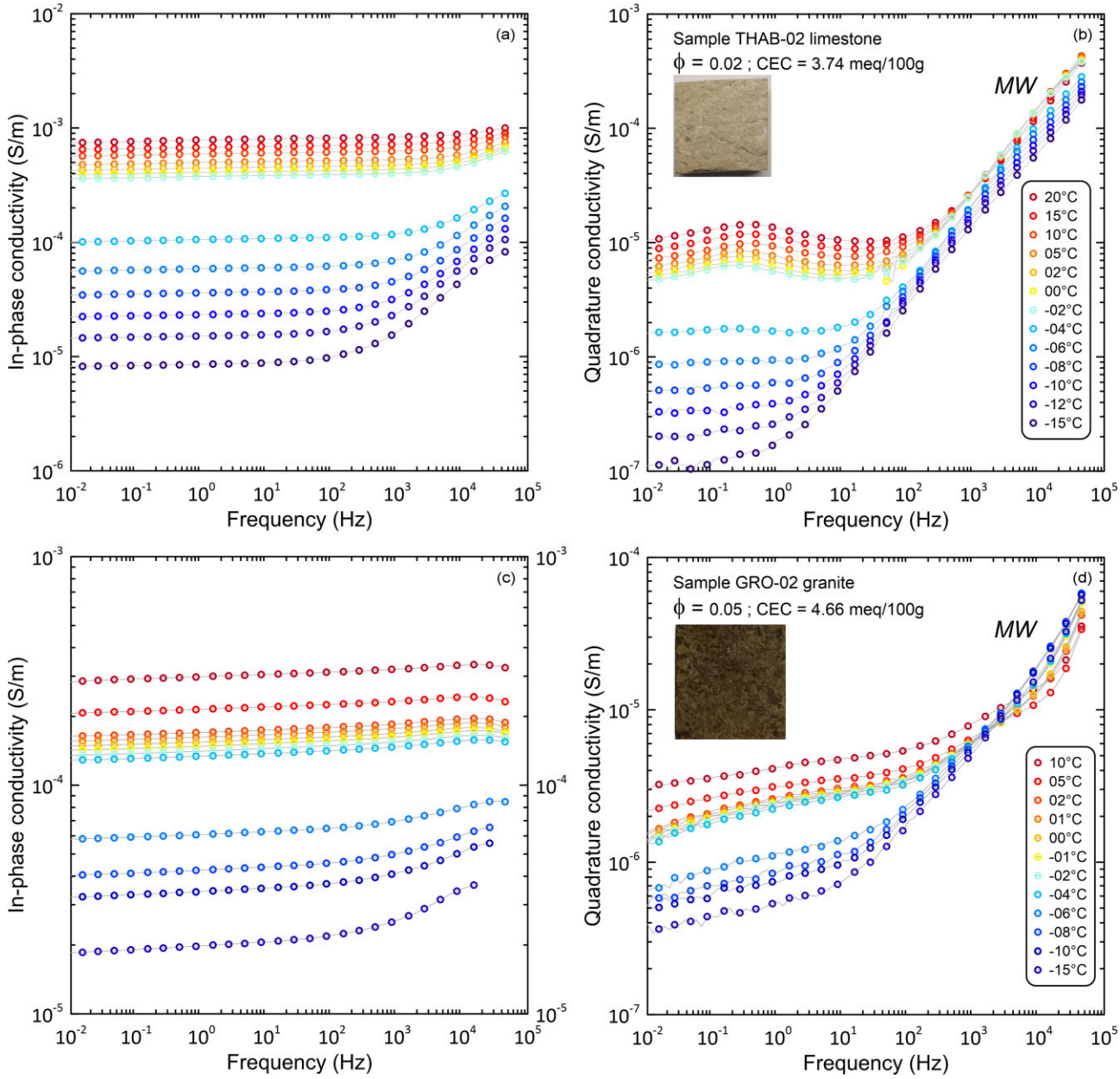

Figure 10. Complex conductivity spectra. (**a**) In-phase conductivity of Sample THAB-02 (limestone). (**b**) Quadrature conductivity of Sample THAB-02 (limestone). (**c**) In-phase conductivity of Sample GRO-02–02 (granite). (**d**) Quadrature conductivity of Sample GRO-02–02 (granite). MW stands for Maxwell–Wagner–Sillars polarization. The lines are just guides for the eyes.

ture. In the next sections, we first characterize the materials above the freezing temperature at ambient temperature (25 °C) and then, we will discuss their properties below the freezing temperature.

4. COMPARISON BETWEEN THE MODEL AND THE EXPERIMENTS AT 25 °C

We first made some comparison between the DSL model and the new set of experimental data at the temperature of 25 °C. In the next section, we will investigate the case of the low-temperature data set. This first step will allow to better characterize the rock samples and to check some of the model predictions.

4.1. Archie's law

The formation factor and surface conductivity of the rock samples were first obtained at room temperature using three salinities (pore water at equilibrium around 0.017 S m^{-1} at 25 °C and two NaCl solutions at 0.5 and 6 S m^{-1} at 25 °C). Above the freezing temperature and assuming water saturation ($\theta = \theta_S = \phi$,θ_S being the water content at saturation), the instantaneous conductivity can be written from eq. (9) (see also Waxman & Smits 1968) as (for $T > 0$ °C),

$$\sigma_1^\infty = \frac{\sigma_w}{F} + \sigma_S^\infty, \tag{30}$$

where $F = \phi^{-m}$ denotes Archie's law (Archie 1942), ϕ (dimensionless) the connected porosity and m (dimensionless) the first Archie exponent. The quantity σ_S^∞ (we use usually σ_S) denotes the

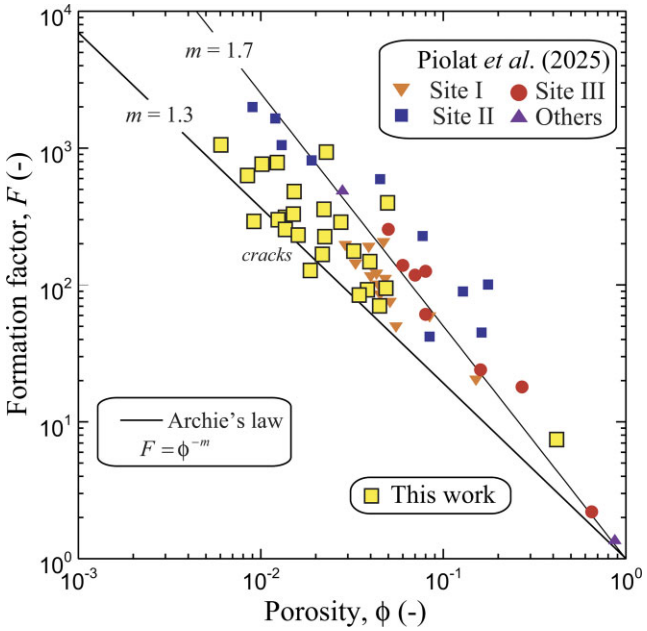

Figure 11. Formation factor versus porosity for the samples used here versus the granites measured by Piolat et al. (2025). The value of the power-law exponent m (called the first Archie exponent or the porosity or cementation exponent) is equal to 1.5 ± 0.2, slightly smaller than the cementation exponent recently reported in Piolat *et al*. (2025)

(instantaneous) surface conductivity while σ_w/F denotes the bulk conductivity assumed to be the dominant conductivity contribution in most studies performed to date. The formation factors are reported as a function of the corresponding (connected) porosities in Fig. 11. At room temperature, we fitted the porosity/formation factor relation (called Archie's law) to obtain the mean value of the Archie's exponent m, which is equal to 1.5 ± 0.3. Low values of the cementation exponent in crystalline rocks may be indicative of the presence of cracks or semiconductors as pyrite or magnetite.

4.2. Importance of surface conductivity

In low-salinity environments, the surface conductivity associated with conduction on the surface of minerals and ice is often neglected and geophysical practitioners use Archie's law as a conductivity equation. This practice that is very common in the literature is generally not supported by any experimental evidence. Assuming Archie's law as a conductivity equation yields,

$$\sigma_1^{\infty} \approx \phi^m \sigma_w. \tag{31}$$

By comparing eq. (31) with eq. (30), this implies that the bulk conductivity dominates the surface conductivity. We are now in the position to validate the first prediction of our model: Surface conductivity is usually dominant in permafrost. Indeed, the pore water conductivity in most environments hosting permafrost in mountainous areas is very low and this supports the idea that not only surface conductivity cannot be neglected but this is likely the dominant conduction mechanism. To validate this preduction, we first consider the value of the pore water conductivity σ_w obtained using melted snow in equilibrium with the crushed mineral grains from the rock samples (see Tables 3 and 4). Then, we compare σ_w/F and σ_S in Fig. 12.

Fig. 12 demonstrates that for most of the rock samples (with the exception of 2 out of 25), surface conductivity is the dominant conduction mechanism or cannot be neglected at 25 °C. What about at lower temperatures? Bulk conductivity decreases quicker with

Table 4. Petrophysical properties of the 25 core samples used in this study. Parameters relevant of the normalized chargeability versus temperature. The experiments are performed at the pore water conductivity σ_w reported in the table at T_0 = 25 °C (the temperature dependence of the liquid pore water conductivity is given in the main text).

Sample	σ_w(25 °C, S m^{-1})	$M_n(T_0)$(S m^{-1})	α_T(°C^{-1})	T_F(°C)	T_C(°C)	θ_r(−)
ETAC-01	0.007	8.70E−06	0.021	−2	−1.90	0.005
ETAC-02	0.010	1.03E−05	0.019	−6	−1.10	0.001
ETAC-03	0.010	2.40E−05	0.021	−6	−0.90	0.002
ETAC-04	0.010	5.00E−05	0.019	−2	−1.92	0.003
ETAC-05	0.007	2.13E−05	0.021	−4	−1.20	0.007
GRO-01	0.018	7.75E−06	0.021	−3	−0.92	0.007
GRO-02	0.019	1.24E−05	0.021	−3	−1.11	0.027
GRO-21a	0.042	1.52E−05	0.021	−2	−1.21	0.007
GRO-21b	0.042	1.04E−05	0.019	−4	−0.61	0.009
KAN-02	0.009	–	–	–	–	–
KAN-03a	0.038	2.11E−06	0.020	−4	−1.00	0.001
KAN-03b	0.038	9.00E−06	0.024	−4	−0.71	0.001
THAB-02	0.015	3.84E−05	0.021	−2	−2.10	0.001
THAB-03	0.015	4.19E−06	0.015	−4	−2.00	0.004
THAB-04	0.017	9.61E−06	0.021	−4	−1.00	0.004
THAB-05	0.017	1.81E−05	0.023	−2	−1.30	0.002
HELB-04	0.013	4.46E−06	0.024	−2	−1.10	0.005
LAURI-01	0.016	3.07E−06	0.026	−2	−0.50	0.003
MON-01	0.020	1.50E−05	0.021	0	−0.70	0.001
MOURTI-02	0.018	5.07E−05	0.019	−3	−1.23	0.019
MONET-01	0.012	1.75E−04	0.022	−2	−0.59	0.045
MONET-02	0.012	4.89E−05	0.017	−2	−2.00	0.013
SISI-01	0.010	9.70E−05	0.022	−3	−0.73	0.014
SISI-02	0.010	1.25E−04	0.022	−3	−0.60	0.010
SISI-03	0.012	9.6 E−06	0.020	−3	−0.82	0.004

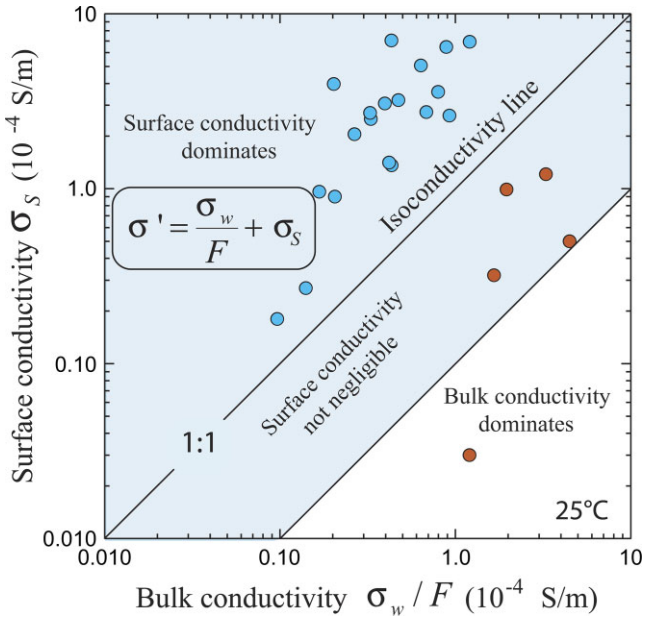

Figure 12. Comparison between the surface conductivity versus the bulk conductivity component. The experimental data indicates that surface conductivity is, for most of the samples the dominant conduction mechanism. For most of the samples (bulk conductivity dominant), the surface conductivity component cannot be totally neglected since the data points are located close to the isoconductivity line (which corresponds to the line for which surface and bulk conductivity are equal, i.e. $\sigma_S = \sigma_w/F$). Most of the data points are located in the dark area for which we cannot neglect surface conductivity at all (at the opposite of what is often claim, without any support, in the literature). This emphasizes once more that the electrical resistivity method cannot be used as a stand-alone method to characterize permafrost.

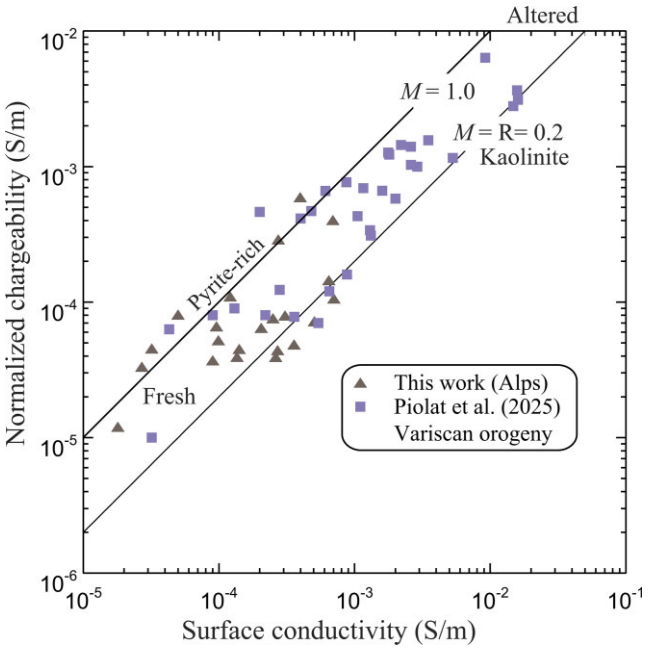

Figure 13. Normalized chargeability (10 mHz–10 kHz) versus surface conductivity (at room temperature 1 Hz) for the data set investigated in this study. The data are comprised between two curves. The first is characterized by $M = 1$ in presence of pyrite and/or magnetite while the second is characterized by $M = R = 0.2$ for kaolinite (the alteration product of the mica and feldspar of granite, see Piolat et al. 2025).

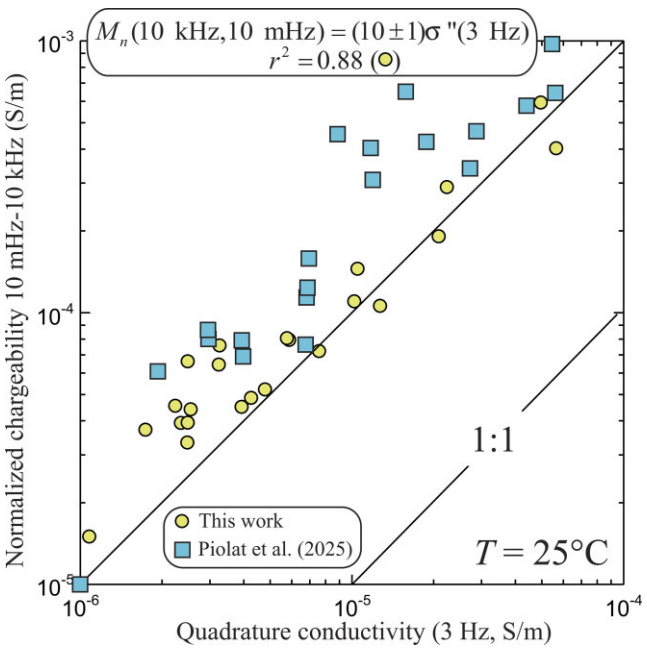

Figure 14. Normalized chargeability (10 mHz–10 kHz) versus quadrature conductivity (at room temperature 3 Hz) for the data set investigated in this study. The measured slope ($\alpha = 10$) is very close to the predicted slope from the Constant Phase Angle model (which leads to yields $\alpha = 11$, see Revil et al 2017a). A comparison is performed with the recent data of Piolat *et al*. (2025). The linear fit is done with the data from this work.

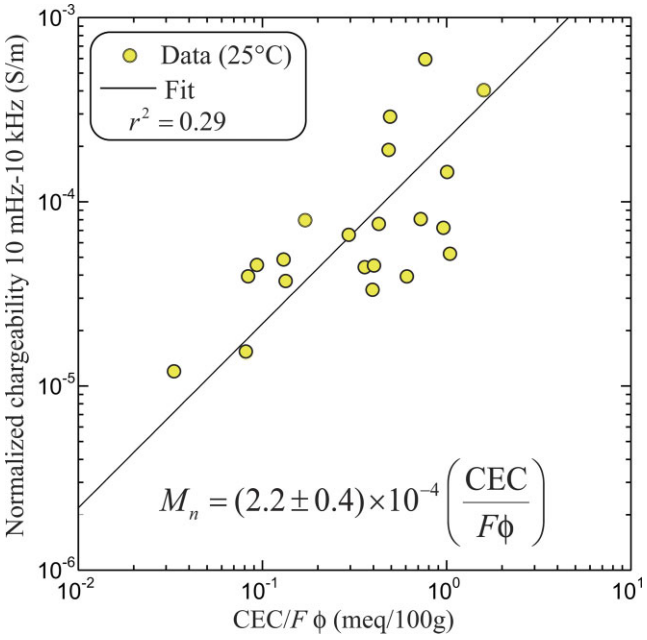

Figure 15. Normalized chargeability (10 mHz–10 kHz) versus the normalized CEC (the CEC divided by the tortuosity of the pore space expressed as the product of the formation factor and the connected porosity) at room temperature for the data set investigated in this study (1 meq/100 g = 963.20 C kg^{-1}).

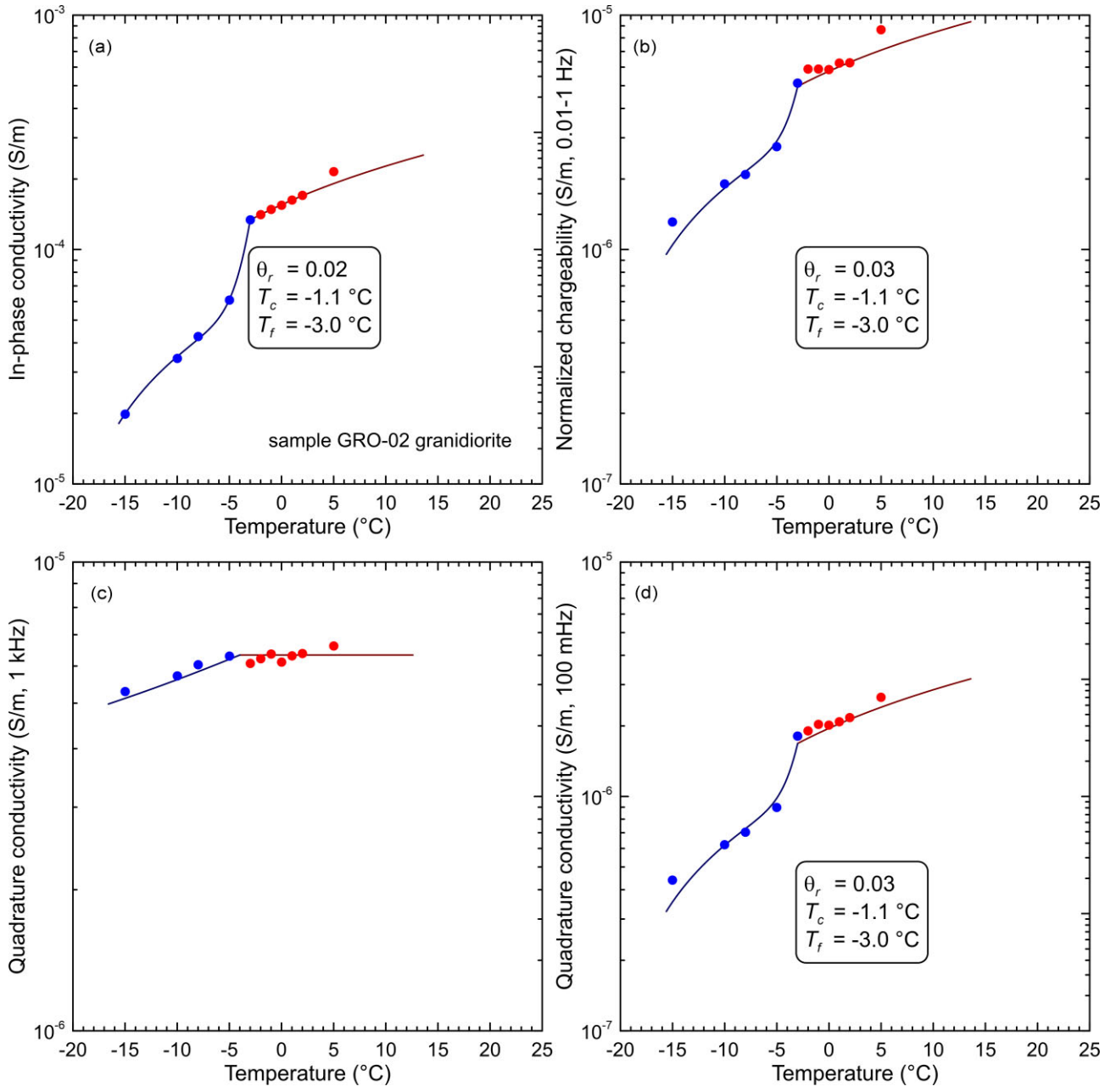

Figure 16. In-phase conductivity and normalized chargeability versus temperature. Experiments performed in closed conditions. (**a**) In-phase conductivity versus temperature. (**b**) Low-frequency normalized chargeability versus temperature. (**c**) High-frequency quadrature conductivity. (**d**) Low-frequency quadrature conductivity.

the saturation than the surface conductivity. Therefore, surface conductivity would be even stronger at low temperatures. Therefore this rules out the use of Archie's law as a conductivity equation in the interpretation of electrical resistivity data and confirmed our first model prediction. This result is in itself a breakthrough if we count the number of papers using Archie's law to interpret electrical resistivity data in permafrost environments. Few works have recognized the importance of complex conductivity in accounting for surface conductivity in permafrost conditions (see recently Maierhofer *et al.* 2024). This proves, once more, that electrical conductivity/resistivity cannot be used as a stand-alone technique in such environments as it was already demonstrated in volcanic and geothermal environments (Revil *et al.* 2017b, c; Piolat *et al.* 2025a). In other words, eq. (31) is not valid whatever the rock considered. Fortunately, surface conductivity and normalized chargeability are proportional to each other as shown in the next section. So induced polarization offer a way to separate bulk and surface contributions.

4.3. Normalized chargeability versus surface conductivity

As demonstrated by Weller *et al.* (2013), surface conductivity and normalized chargeability can be proportional to each other. Such proportionality is well-explained by the DSL model proposed by

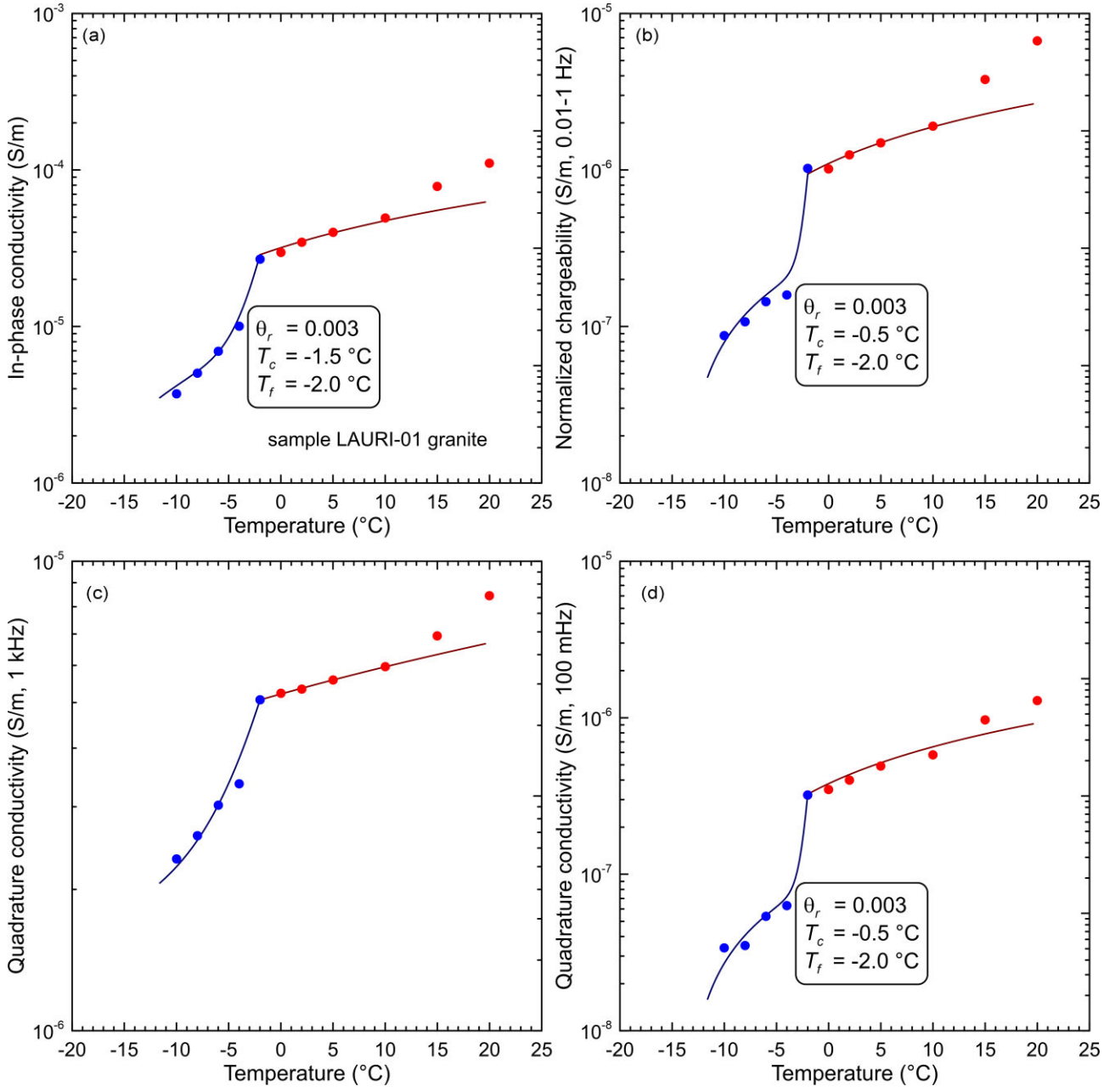

Figure 17. In-phase conductivity and normalized chargeability versus temperature. Experiments performed in closed conditions. (**a**) In-phase conductivity versus temperature. (**b**) Low-frequency normalized chargeability versus temperature. (**c**) High-frequency quadrature conductivity. (**d**) Low-frequency quadrature conductivity.

Revil (2012, 2013). Fig. 13 shows this is the case for the data set used in this work. This explains why making induced polarization together with electrical resistivity measurements is very important. It can be used to separate the bulk conductivity from the surface conductivity in all types of environments including in ice-rich environments for which the conductivity of the pore water is very small, on the same order of magnitude as the surface conductivity.

4.4. Normalized chargeability versus quadrature conductivity

In Fig. 14, we check that the normalized chargeability and the quadrature conductivity are proportional to each other at 25 °C. The normalized chargeability is determined as the difference between the in-phase conductivity at 10 kHz and 10 mHz while the quadrature conductivity is determined at the geometric mean of the two frequencies (3 Hz in the present case). According to Revil *et al.* (2017a, see their Appendix A), the two quantities characterizing polarization are related to each other by,

$$M_n(f_1, f_2) \approx \alpha \, \sigma''\left(\sqrt{f_1 f_2}\right), \tag{32}$$

where $\alpha \approx (2/\pi) \ln A$ and A denotes the ratio between the frequency $f_2 (> f_1)$ and frequency f_1. In the present case, the number of decades separating the low and high frequencies is 6, this yields $\alpha = 11$ while we measure $\alpha = 10$ in Fig. 14. There is therefore a good agreement between the observations and the model prediction.

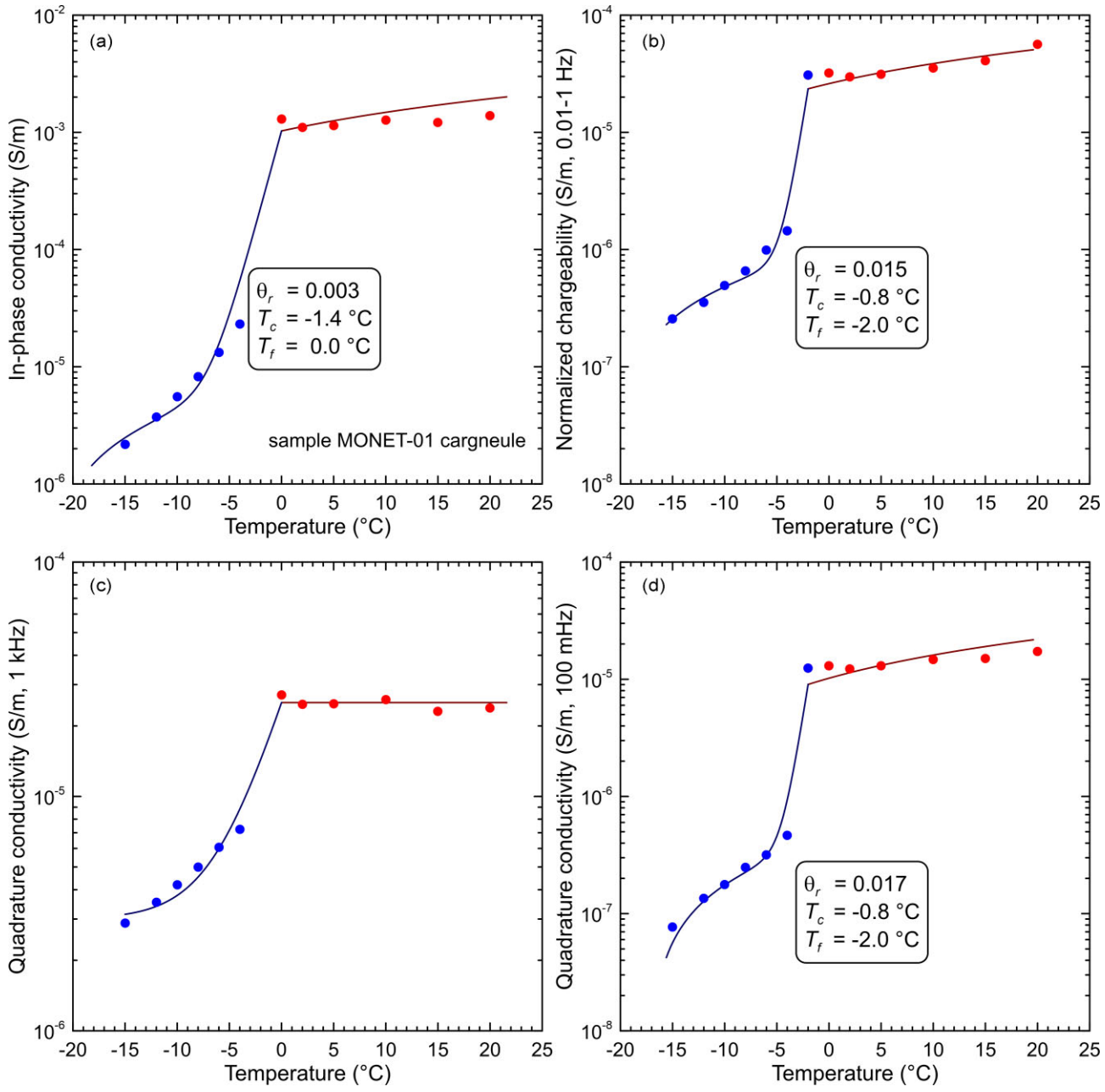

Figure 18. In-phase conductivity and normalized chargeability versus temperature. Experiments performed in closed conditions. (**a**) In-phase conductivity versus temperature. (**b**) Low-frequency normalized chargeability versus temperature. (**c**) High-frequency quadrature conductivity. (**d**) Low-frequency quadrature conductivity.

4.5. Dependence on the CEC

Still at 25 °C, we can check the effect of the CEC upon the surface conductivity or normalized chargeability data (both being proportional to each other). Fig. 15 demonstrates that the normalized chargeability is proportional to the CEC divided by the tortuosity of the pore space (product of the formation factor by the porosity) as predicted by the DSL model. We have approximately $M_n(10\text{kHz}, 10\text{mHz}) \approx M_n$ and the fit of the data yields,

$$M_n \approx (2.2 \pm 0.4 \times 10^{-4}) \frac{\text{CEC}}{F\phi}. \quad (33)$$

Since we have $M_n = \rho_g \lambda \, \text{CEC}/F\phi$ and using CEC = 1 meq/100 g = 963.20 C kg^{-1} (see Section 3.1), using the slope of the trend reported in eq. (33), we obtain $\lambda(\text{Na}^+, 25°\text{C}) = 8.8 \pm 0.2 \times 10^{-11}$ m^{-2} s^{-1} V^{-1}. Since $B(\text{Na}^+, 25\ °\text{C}) = 3.1 \pm 0.3 \times 10^{-9}$ m^{-2} s^{-1} V^{-1}, we have $R \equiv \lambda/B = 0.03$.

4.6. Influence of temperature above the freezing point

Above the freezing point, the in-phase conductivity, the surface conductivity, the normalized chargeability and the quadrature conductivity has the same temperature dependence, which

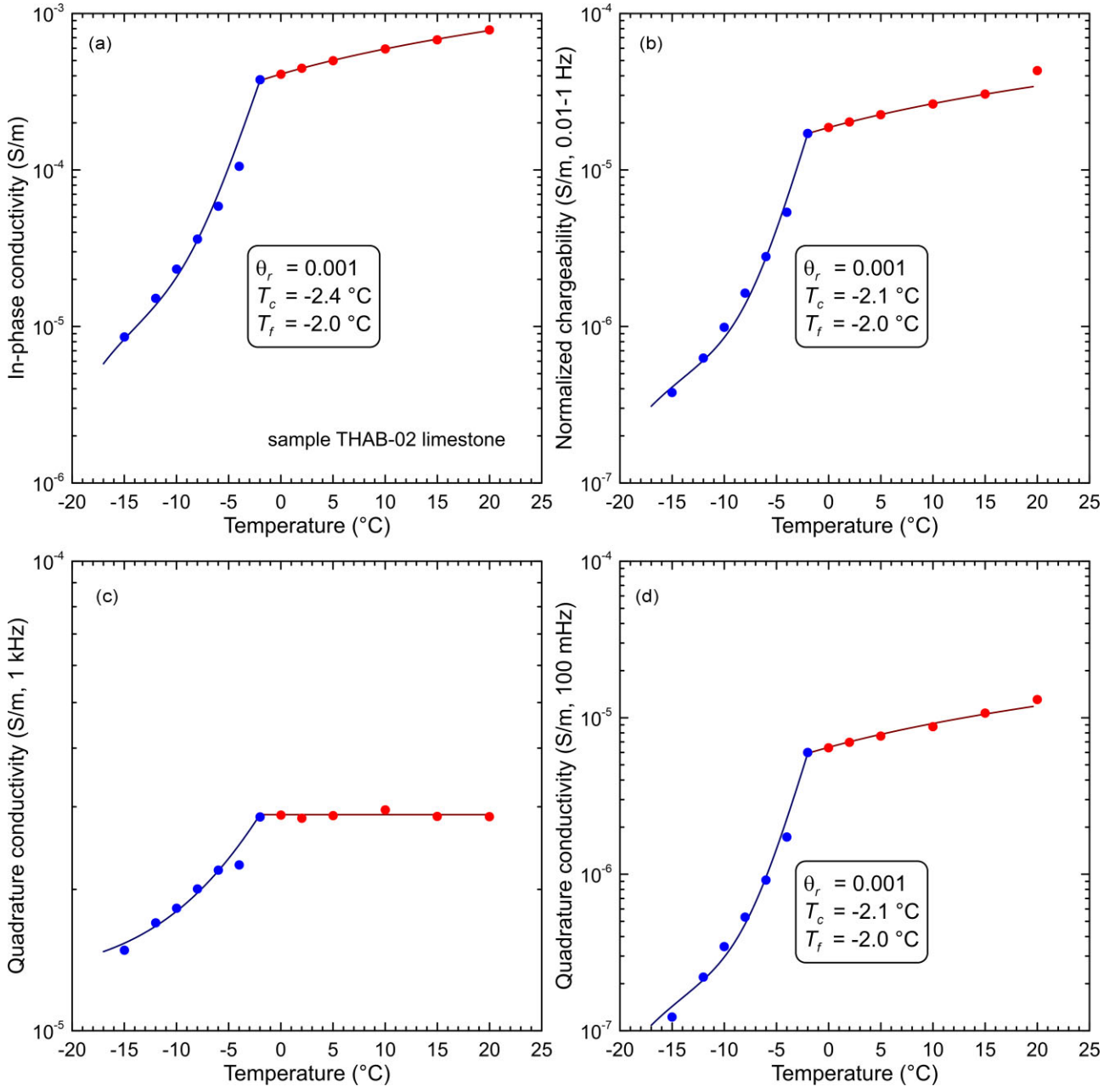

Figure 19. In-phase conductivity and normalized chargeability versus temperature. Experiments performed in closed conditions. (**a**) In-phase conductivity versus temperature. (**b**) Low-frequency normalized chargeability versus temperature. (**c**) High-frequency quadrature conductivity. (**d**) Low-frequency quadrature conductivity.

is dictated by the temperature dependence of the ionic mobilities with temperature. This temperature dependence is the one shown in eqs (15) to (17), that is a linear temperature dependence with a coefficient $\alpha_w \approx 0.022 \pm 0.003/°C$ (see for instance Figs 16a and b). This is confirmed by the temperature dependence shown by the plain lines above the freezing temperature and at low frequencies (below 1 kHz). For the quadrature conductivity and in agreement with the model described above, there is no temperature dependence of the quadrature conductivity when the Maxwell–Wagner–Sillars polarization mechanism dominates the overall polarization response of the rock (see Fig. 16c).

5. INFLUENCE OF THE TEMPERATURE BELOW THE FREEZING TEMPERATURE

5.1. Adequacy of the exponential freezing curve

The next and final step of our investigation is to check the model prediction for the effect of the temperature below the freezing point. We use eqs (12) to (18) to fit the data of the in-phase conductivity, quadrature conductivity and normalized chargeability versus temperature. Figs 16–19 show that below the freezing point, we can generally fit the data with our physics-based model (including the effect of the exponential freezing law). The resulting fitting parameters for the freezing curve are reported in Tables 3 and 4. This

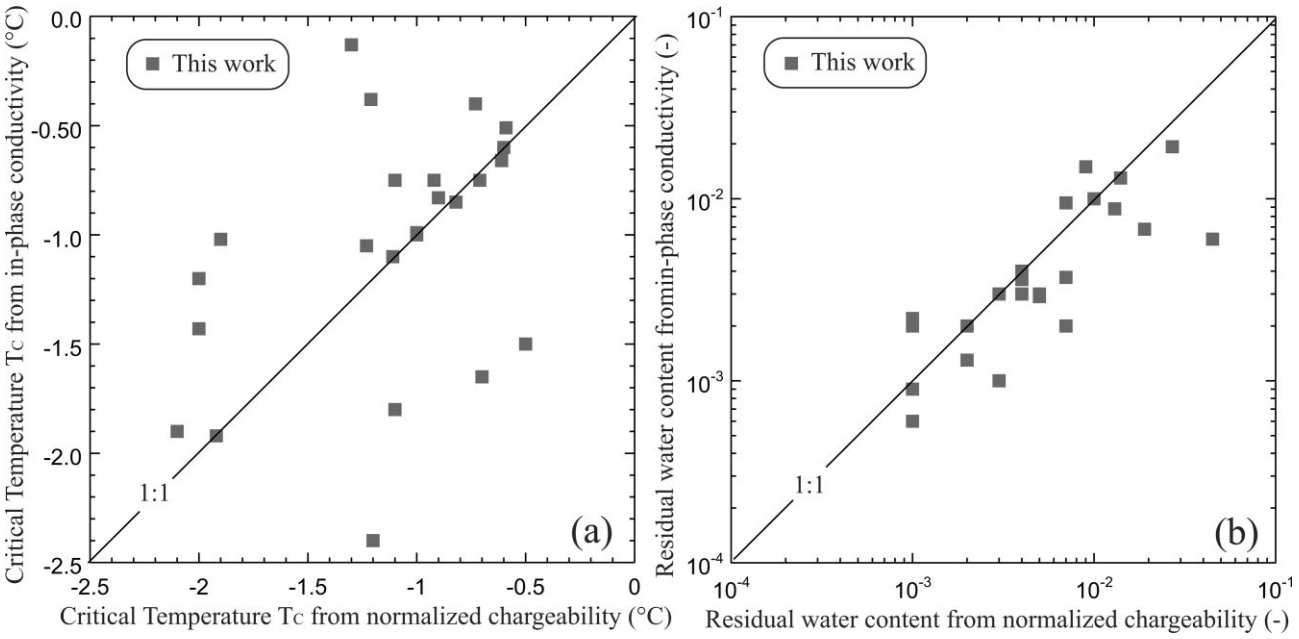

Figure 20. Critical temperature T_C (°C) and residual water content θ_r (dimensionless) of eq. (18). (**a**) Determination from the in-phase conductivity versus temperature data. (**b**) Determination from the normalized chargeability versus temperature data.

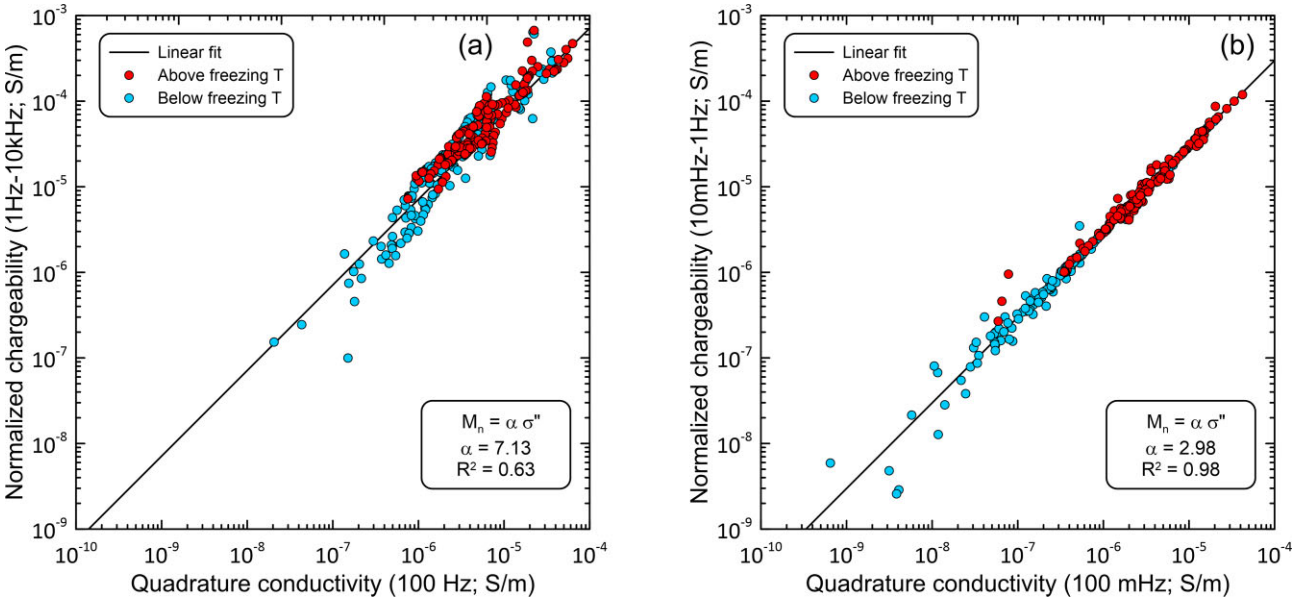

Figure 21. Partial normalized chargeability versus quadrature conductivity for the low- and high-frequency ranges. (**a**) High frequency range (1 Hz–10 kHz). The quadrature conductivity is determined at the geometrical mean of the two frequencies used to determine the normalized chargeability (100 Hz). (**b**) Low-frequency range (10 mHz–1 Hz). The quadrature conductivity is determined at the geometrical mean of the two frequencies used to determine the normalized chargeability (100 mHz).

provides a database to model the freezing curve and the resulting resistivity and induced polarization properties in field conditions for different lithologies. Fig. 20 provides a comparison between the fitted parameters for the freezing curve obtained by fitting either the conductivity data or the normalized chargeability data. They are generally consistent. Our approach is physics-based and may appear therefore better than empirical fitting procedure proposed by some authors.

The exponential freezing curve introduced by Duvillard *et al.* (2018) is making a great job in capturing the temperature dependence of the conductivity, normalized chargeability and quadrature conductivity below the freezing point. Since this curve has a physical meaning in terms of pore size distribution, it should be compared to capillary pressure curves. This would establish an additional bridge between properties.

5.2. Evidences of direct ice polarization?

The last question to handle is to see if there is any trace of the polarization of the ice in our data set. As shown in Fig. 4(c), the polarization of the surface of ice crystals is a relatively high-frequency

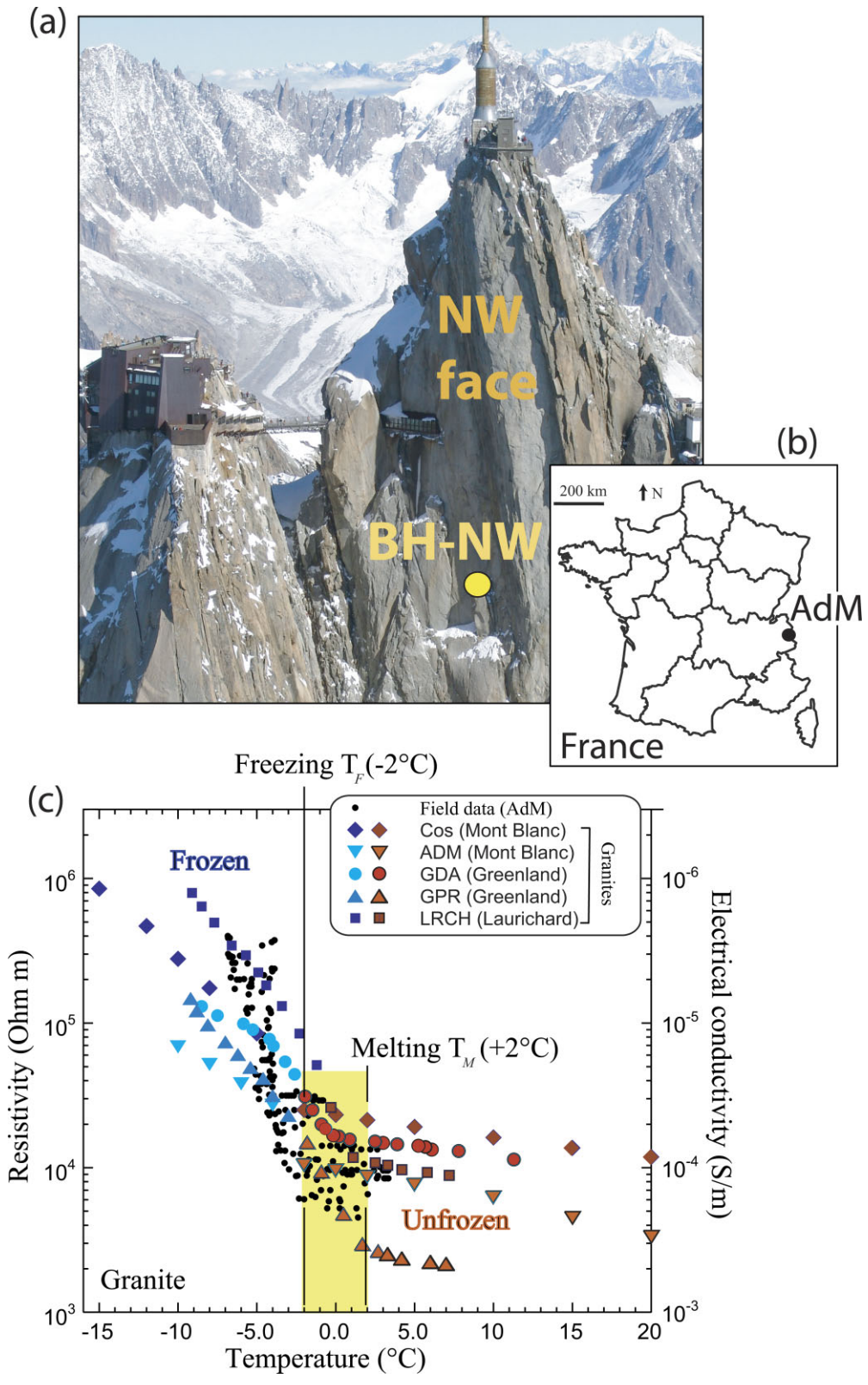

Figure 22. Comparison between field and experimental data. (**a**) Picture of the Aiguille du Midi (AdM, 3842 m a.s.l.) showing the position of the borehole in which the temperature measurements are taken. (**b**) Position of the Aiguille du Midi in France. (**c**) Comparison between the observed resistivity/temperature changes at the Aiguille du Midi and the laboratory data using five core samples of granite in freezing and thaw conditions. The light-covered area corresponds to the transition zone in between the melting and freezing temperatures. The pore water conductivity used for the experiment (in equilibrium with the mineral paragenesis) is 150 ± 50 μS cm^{-1} (25 °C).

polarization process (relaxation frequency around 1 kHz). There is no dispersion observed below 1 Hz. This implies that in presence of ice, we expect to see the direct effect of ice polarization only above 1 Hz and possibly through a superposition of Maxwell–Wagner–Sillars and ice polarization, which may make the deconvolution of the two effects rather difficult. Figs 21(a) and (b) provide a way to see the effect of ice.

Fig. 21(a) analyse the relationship between the normalized chargeability in the high-frequency range (1 Hz–10 kHz, 4 orders of magnitude) versus the quadrature conductivity at the geometrical mean of the two frequencies (100 Hz). We observe that the data show some dispersion below the freezing point (different slope). The slope of the trend is $\alpha = 7$ while eq. (32) with $\alpha \approx (2/\pi) \ln A$ predict a slope with $\alpha \approx 6$ using the prescribed frequencies. There is therefore a small discrepancy between the model prediction and the observations that can be possibly attributed to the presence of ice.

Fig. 21(b) shows the relationship between the normalized chargeability in the low-frequency range (10 mHz–1 Hz, 2 orders of magnitude) versus the quadrature conductivity at the geometrical mean of the two frequencies (0.1 Hz). We see no change of the slope above and below the freezing temperature indicating no effect of the ice itself. Furthermore, the slope of the trend is $\alpha = 3.0$ while eq. (32) predict a slope of 2.9. There is therefore no discrepancy between the model prediction and the observations.

6. RESISTIVITY: FIELD VERSUS LABORATORY DATA

We provide in this section a comparison between laboratory and field data to start bridging the petrophysical results obtained in this section with the field data, which will be the main research target of the companion paper. We end our analysis with the data reported in Fig. 22 comparing field data in terms of resistivity versus temperature and laboratory data on core samples. The Aiguille du Midi is equipped of four 10-m-depth boreholes in four different sun-exposure. In this study, we use the borehole installed on the NW face of the Central Pillar. It was drilled in September 2009, normal to the surface of a west facing (270°N) and vertical (90°) rockwall at an elevation of 3745 m, that is c. 80 m below the anthropogenic disturbances. The borehole is equipped with a 15 sensors YSI 44031 Stump ForaTech AG thermistors (accuracy $\pm$ 0.1 °C) thermistor chain that is associated with a Campbell CR1000 logger running with a solar pannel. Temperature is registered every 3 hr at depths of 0.3, 0.5, 0.7, 0.9, 1.1, 1.4, 1.7, 2, 2.5, 3, 4, 5, 7, 9 and 10 m. The monitoring as started in December 2009 and is running since then without any specific maintenance (other boreholes have however experiences various sensor breaks and replacement). At 2.5 m, the borehole crosses an open network of fractures and cracks that causes air ventilation and a local cooling (Magnin *et al*. 2015). The active layer thickness (i.e. maximum depth of the 0 °C isotherm) interpolated between sensors is ranging between 1.26 m (2014) and 2.72 m (2022). It has increased by about 1.05 m per decade over the period 2011–2020, while the temperature at 10-m-depth has increased by 0.96 °C over the same period, reaching −4 °C in average over the recent years (Magnin *et al.* 2024). It is noteworthy that at 10-m-depth, seasonal oscillations are still important (about 1 °C amplitude) and that the warmest period is generally in January while the lowest temperature is generally registered in June.

Fig. 22 offers a comparison between the field data recorded at this borehole at ADM (including monitoring of electrical resistivity with electrical resistivity tomography) and experimental data performed with core samples. The temperature/resistivity fluctuations observed in the field are consistent with experimental data obtained for freezing and thaw conditions on several samples of granites. This offers a way to include the geophysical data and numerical modelling of freeze and thaw to get 4-D temperature changes at such a site using machine learning algorithms, numerical modelling of the heat and temperature, and a combination of *in situ* and geophysical measurements (Abdulsamad *et al.* 2025). In the second paper of this series, we will extend such comparison to induced polarization measurements obtained in field conditions to better see how laboratory and field results are consistent.

7. CONCLUSIONS

We have developed a new database of experimental data using 25 mostly crystalline rock samples in a broad temperature range between approximately +15 °C/+20 °C to −15 °C. The complex conductivity spectra are performed in the frequency range 1 mHz–45 kHz with a high-precision impedance meter. The rock samples have been characterized by measuring their connected porosity and cation exchange capacity (the CEC is in the range 0.1 to 7 meq/100 g, i.e. covering nearly two orders of magnitude). The DSL model was used to make five model predictions regarding relationships between the electrical properties of interest and their chemical and textural characteristics. We have successfully tested these five predictive relationships. The model will be tested on field data in the second paper of this series using two field data sets in crystalline rocks and a third one in sedimentary rocks to show the effect of the ice content on the induced polarization properties in permafrost conditions. The good comparison between experimental data and field data for the resistivity at the Aiguille du Midi test site indicates that surface conductivity dominates the field response in agreement with our petrophysical analysis. Our paper underlines the strong role of surface conductivity in the case of permafrost in agreement with those of Kozhevnikov & Antonov (2012) using time-domain electromagnetic data applied to permafrost in field conditions.

DATA AVAILABILILY

The data used in this manuscript are available upon request to the corresponding author.

ACKNOWLEDGMENTS

We thank the CNRS for supporting this work, E. Zimmerman for the construction of the two ZELSIP04-V02 impedance meters used in this work. We thank G. Ménard, F. Abdulsamad, J. Bock and X. Bodin for fruitful discussions. The PhD thesis of Jessy Richard was supported by a CIFRE grant with Naga Geophysics. We also thank Agence National de la Recherche (ANR) (grant # ANR-19-CE01-0018 WISPER) for the acquisition of the data at Aiguille du Midi and the Ministère de la Transition Ecologique for the Post-doc of Feras Abdulsamad and the funding for some of the laboratory experiments. The field campaigns to collect samples from Greenland were funded by the Nunatsinni Ilisimatusarnermik Siunnersuisoqatigiit (Greenland Research Council) and the Nordforsk ColdHUB project. The equipment used in this project was obtained thanks to the funding of the Auvergne-Rhône-Alpes region and FEDER through the IRICE project with the help of IRISK. IRISK is thanked for its strong support and fruitful discussions regarding

gravitational instabilities over the years and especially M. Bernard and F. Nicot for their strong encouragements over the past 7 yr. A. Revil thanks S. Missmahl for inspiration. This paper is dedicated to Gary Olhoeft, who first measured conductivity and dielectric permittivity of permafrost over a broad range of frequencies and drew the attention to the scientific community to their remarkable dispersion phenomena. We thank the Editor and two anonymous referees for their useful comments used to improve the manuscript.

REFERENCES

Abdulsamad, F. *et al.* 2020. Complex conductivity of graphitic schists and sandstones, *J. Geophys. Res.: Solid Earth,* **124,** 8223–8249. .

Abdulsamad, F. *et al.* 2025. *Rockwall Permafrost Dynamics Evidenced by Automated Electrical Resistivity Tomography at Aiguille du Midi (3842 m a.s.l., French Alps),* EGUsphere..

Anderson, R., Tohidi, B. & Webber, J.B.W., 2009. Gas hydrate growth and dissociation in narrow pore networks: capillary inhibition and hysteresis phenomena, *Geol. Soc. London Spec. Publ.,* **319**(1), 145–159..

Aran, D., Maul, A. & Masfaraud, J., 2008. A spectrophotometric measurement of soil cation exchange capacity based on cobaltihexamine chloride absorbance, *C. R. Geosci.,* **340**(12), 865–871.

Archie, G.E., 1942. The electrical resistivity log as an aid in determining some reservoir characteristics, *Trans. AIME,* **146,** 54–62

Auty, R.P. & Cole, R.H., 1952. Dielectric properties of ice and solid D2O, *J. Chem. Phys.,* **20**(8), 1309–1314.

Bittelli, M., Flury, M. & Roth, K., 2004. Use of dielectric spectroscopy to estimate ice content in frozen porous media, *Water Resour. Res.,* **40**(4), 1–11.

Bullemer, B. & Riehl, N., 1966, Bulk and surface conductivity of ice, *Solid State Commun.,* **4**(9), 447–448.

Caranti, J.M. & Illingworth, A.J., 1983. Frequency dependence of surface conductivity of ice, *J. Phys. Chem.,* **87**(21), 4078–4083.

Casotti, C., Revil, A., Abdelfattah, M., Guerini, M., Hoblea, F., Ménard, G., Su, Z., Qiang, S., Berthet, J., Laroche, P., Lansigu, C., Houtteville, T. & Côme, J.M., 2025a. Induced polarization applied to landslides. Part 1: imaging hydraulic barriers. *Geophysical Journal International* **242,** 1–26, https://doi.org/10.1093/gji/ggaf218.

Cathala, M. *et al.* 2024a. Predisposing, triggering and runout processes at a permafrost-affected rock avalanche site in the French Alps (Étache, June 2020), *Earth Surface Processes and Landforms,* pp. 1–27.

Cathala, M. *et al.* 2024b. Assessing the role of permafrost in the preconditioning and triggering factors of the September 2020 Crête des Grangettes rockfall (southern French Alps), *Géomorphol.: Relief Process. Environ.,* **30,** 3.

Chen, C., Liu, Y., Wang, Y., Su, L. & Cheng, Y., 2025. Investigation of coupled thermo-hydro-mechanical processes on soil slopes in seasonally frozen regions, *Cold Reg. Sci. Technol.,* **229,** 104 356..

Cole, K.S. & Cole, R.H., 1941. Dispersion and absorption in dielectrics. I: alternating current characteristics, *J. Chem. Phys.,* **9,** 341–351.

Coperey, A., Revil, A., Abdulsamad, F., Stutz, B., Duvillard, P.A. & Ravanel, L., 2019. Low-frequency induced polarization of porous media undergoing freezing: preliminary observations and modeling, *J. Geophys. Res.: Solid Earth,* **124,** 4523–4544..

Cosenza, P., Ghorbani, A., Revil, A., Zamora, M., Schmutz, M., Jougnot, D. & Florsch, N., 2008. A physical model of the low-frequency electrical polarization of clay-rocks, *J. geophys. Res.,* **113,** B08204..

Daigle, H., 2021. Structure of the electrical double layer at the ice–water interface, *J. Chem. Phys.,* **154,** 214 703..

Dou, S., Nakagawa, S., Dreger, D. & Ajo-Fanklin, J., 2016, A rock-physics investigation of unconsolidated saline permafrost: p-wave properties from laboratory ultrasonic measurements, *Geophysics,* **81**(1), WA233–WA245..

Duvillard, P.A. *et al.* 2025, La chapelle du Thabor (3165 m, Hautes-Alpes), un patrimoine sensible à l'évolution du permafrost de montagne, the Thabor chapel (3165 m.a.s.l., Hautes-Alpes), a heritage site vulnerable to changes in mountain permafrost, *Géomorphol. Relief Process. Environ.,* **30**(3)..

Duvillard, P.A., Magnin, F., Revil, A., Legay, A., Ravanel, L., Abdulsamad, F. & Coperey, A., 2021. Determining 2D temperature distribution in a permafrost-affected rock ridge from electrical conductivity tomography, *Geophys. J. Int.,* **225,** 1207–1221doi: 461 10.1093/gji/ggaa597.

Duvillard, P.A., Revil, A., Soueid Ahmed, A., Qi, Y., Coperey, A. & Ravanel, L., 2018. Three-dimensional electrical conductivity and induced polarization tomography of a rock glacier, *J. geophys. Res.,* **123,** 9528–9554.

Eigen, M. & de Maeyer, L., 1958. Self-dissociation and protonic charge transport in water and ice, *Proc. R. Soc. London Ser. A Math. Phys. Sci.,* **247**(1251), 505–533.

Fereydooni, H., Gruber, S., Cronmiller, D. & Stillman, D. 2024. Utilizing spectral induced polarization to identify the ice core of a pingo: a case study in Haines Junction, Yukon, Canada, In: *12th International Conference on Permafrost, 16-20 June 2024, Vol. 1,* pp. 87–93, eds, Beddoe, R.A. & Karunaratne, K.C., International Permafrost Association.

Fereydooni, H., Gruber, S., Stillman, D. & Cronmiller, D., 2025. Detecting ground ice in warm permafrost with the dielectric relaxation time from SIP observations, *EGUsphere, Preprint egusphere-2025-1801*.

Gariano, S.L. & Guzzetti, F., 2016. Landslides in a changing climate, *Earth Sci. Rev.,* **162,** 227–252..

Hartmeyer, I., Delleske, R., Keuschnig, M., Krautblatter, M., Lang, A., Schrott, L. & Otto, J.-C., 2020. Current glacier recession causes significant rockfall increase: the immediate paraglacial response of deglaciating cirque walls, *Earth Surf. Dynam.,* **8,** 729–751.

Hauck, C. & Vonder Mühll, D., 2003. Inversion and interpretation of two-dimensional geoelectrical measurements for detecting permafrost in mountainous regions, *Permafr. Periglac. Process.,* **14,** 305–318..

Hauck, C., 2002. Frozen ground monitoring using DC resistivity tomography, *Geophys. Res. Lett.,* **29,** 12–12..

Hauck, C., Vonder Mühll, D. & Maurer, H., 2003. Using DC resistivity tomography to detect and characterize mountain permafrost, *Geophys. Prospect.,* **51,** 273–284..

Herring, T. *et al.* 2023. Best practices for using electrical resistivity tomography to investigate permafrost, *Permafr. Periglac. Process*., **34,** 494–512.

Herring, T., Cey, E. & Pidlisecky, A., 2019. Electrical resistivity of a partially saturated porous medium at subzero temperatures, *Vadose Zone J.,* **18**(1), 1–11..

Herring, T., Pidlisecky, A. & Cey, E., 2021. Removing the effects of temperature on electrical resistivity tomography data collected in partially frozen ground: limitations and considerations for field applications, *Vadose Zone J.,* **20,** e20146..

Hou, Y., Sun, X., Dou, M. & Lu, C., 2021. Cellulose nanocrystals facilitate needle-like ice crystal growth and modulate molecular trgeted ice crystal nucleation, *Nanoletters,* **21,** 1..

Jaccard, C., 1967. Electrical conductivity of the surface layer of ice, *Physics of Snow and Ice: Proceedings,* **1**(1), 173–179.

Jacquemart, M. *et al.* 2024. Detecting the impact of climate change on alpine mass movements in observational records from the European Alps, *Earth Sci. Rev.,* **258,** 104 886.

Jia, H., Ding, S., Wang, Y., Zi, F., Sun, Q. & Yang, G., 2019, An NMR-based investigation of pore water freezing process in sandstone, *Cold Reg. Sci. Technol.,* **168,** 102 893..

Keuschnig, M., Krautblatter, M., Hartmeyer, I., Fuss, C. & Schrott, L., 2017. Automated electrical resistivity tomography testing for early Warning in unstable permafrost rock walls around alpine infrastructure, *Permafr. Periglac. Process*., **28,** 158–171.

Kozhevnikov, N.O. & Antonov, E.Y., 2012. Fast-decaying inductively induced polarization in frozen ground: a synthesis of results and models, *J. Appl. Geophys.,* **82,** 171–183.

Kozhevnikov, N.O., 2022. On the association between fast induced polarization in frozen rocks and dielectric polarization of ice, *Geophys. Prospect.,* **70,** 1–8.

Krautblatter, M., Verleysdonk, S., Flores-Orozco, A. & Kemna, A., 2010. Temperature-calibrated imaging of seasonal changes in permafrost rock

walls by quantitative electrical resistivity tomography (Zugspitze, German/Austrian Alps), *J. geophys. Res.,* **115,** F02003.
Kulessa, B., 2007. A Critical review of the low-frequency electrical properties of ice sheets and slaciers, *JEEG,* **12**(1), 23–36.
Limbrock, J.K., Weigand, M. & Kemna, A., 2025. Temperature dependence of the low-frequency electrical properties of partially frozen rocks, *J. Geophys. Res.: Solid Earth,* **130,** e2024JB030870..
Luo, H., Jost, A., Thiesson, J., Mendieta, A., Léger, E. & Jougnot, D., 2025. Induced polarization of clay under freeze-thaw cycling and desiccation processes: effect of surface cracking propagation, *Geophys. Res. Lett.,* **52,** e2024GL113424
Luo, H.L., Jougnot, D., Jost, A., Teng, J.D., Mendieta, A., Lin, G. & Thanh, L.D., 2024. Predicting the electrical conductivity of partially saturated frozen porous media, a fractal model for wide ranges of temperature and salinity, *Water Resour. Res.,* **60**(3), e2023WR034845..
Mader, H.M., 1992, Observations of the water-vein system in polychrystalline ice, *J. Glaciol.,* **38**(130), 333–347.
Maeno, N. & Nishimura, H., 1978. The electrical properties of ice surfaces, *J. Glacial.,* **21**(85), 193–205..
Magnin, F., Krautblatter, M., Deline, P., Ravanel, L., Malet, E. & Bevington, A., 2015a. Determination of warm, sensitive permafrost areas in near–vertical rockwalls and evaluation of distributed models by electrical resistivity tomography, *J. Geophys. Res.: Solid Earth,* **120,** 745–762.
Magnin, F., Deline, P., Ravanel, L., Noetzli, J. & Pogliotti, P., 2015b. Thermal characteristics of permafrost in the steep alpine rock walls of the Aiguille du Midi (Mont Blanc Massif, 3842 m a.s.l), *The Cryosphere,* **9,** 109–121.
Magnin, F., Ravanel, L., Bodin, X., Deline, P., Malet, E., Krysiecki, J.-M. & Schoeneich, P., 2024. Main results of permafrost monitoring in the French Alps through the *PermaFrance* network over the period 2010–2022, *Permafr. Periglac. Process.,* **35**(1), 3–23..
Magnin, F., Westermann, S., Pogliotti, P., Ravanel, L., Deline, P. & Malet, E., 2017. Snow control on active layer thickness in steep alpine rock walls (Aiguille du Midi, 3842 m a.s.l., Mont Blanc massif), *Catena,* **149,** 648–662..
Maierhofer, T. *et al.* 2024. Spectral induced polarization imaging to monitor seasonal and annual dynamics of frozen ground at a mountain permafrost site in the Italian Alps, *Cryosphere,* **18**(7), 3383–3414..
Maierhofer, T., Hauck, C., Hilbich, C., Kemna, A. & Flores-Orozco, A., 2022. Spectral Induced Polarization imaging to investigate an ice-rich mountain permafrost site in Switzerland, *The Cryosphere,* **16,** 1903–1925.
Marcer, M., *et al.* 2025. Regional patterns of mountain permafrost in Central West Greenland: a comparison between field data and regional models, *Permafr. Periglac.Process* in press in.
Marcer, M., Duvillard, P.-A., Tomaškovičová, S., Nielsen, S.R., Revil, A. & Ingeman-Nielsen, T., 2024. Modelling present and future rock wall permafrost distribution in the Sisimiut mountain area, West Greenland, *The Cryosphere,* **18,** 1753–1771.
Misra, S., Torres-Verdín, C., Revil, A., Rasmus, J. & Homan, D., 2016a. Interfacial polarization of disseminated conductive minerals in absence of redox-active species. Part 1: mechanistic model and validation, *Geophysics,* **81**(2), E139–E157.
Misra, S., Torres-Verdín, C., Revil, A., Rasmus, J. & Homan, D., 2016b. Interfacial polarization of disseminated conductive minerals in absence of redox-active species. Part 2. Effective complex conductivity and dielectric permittivity, *Geophysics,* **81**(2), E159–E176.
Mollaret, C., Hilbich, C., Pellet, C., Flores-Orozco, A., Delaloye, R. & Hauck, C., 2019. Mountain permafrost degradation documented through a network of permanent electrical resistivity tomography sites, *The Cryosphere,* **13,** 2557–2578.
Moser, C., Morra di Cella, U., Hauck, C. & Flores Orozco, A., 2025, Spectral induced polarization survey for the estimation of hydrogeological parameters in an active rock glacier, *The Cryosphere,* **19,** 143–171..
Myhra, K.S., Westermann, S. & Etzelmüller, B., 2017. Modelled distribution and temporal evolution of permafrost in steep rock walls along a latitudinal transect in Norway by CryoGrid 2D, *Permafr. Periglac. Process.,* **28**(1), 172–182..
Offer, M., Weber, S., Krautblatter, M., Hartmeyer, I. & Keuschnig, M., 2025. Pressurised water flow in fractured permafrost rocks revealed by borehole temperature, electrical resistivity tomography, and piezometric pressure, *The Cryosphere,* **19,** 485–506 2025.
Olhoeft, G.R., 1981a. Electrical properties of granite with implications for the lower crust, *J. geophys. Res.,* **86**(B2), 931–936.
Olhoeft, G.R., 1981b. Electrical properties of rocks, in *Physical Properties of Rocks and Minerals,* pp. 257–297, eds, Touloukian, Y. S., Judd, W. R. & Roy, R. F., McGraw Hill.
Petrenko, V.F. & Maeno, N., 1987. Ice field transistor, *J. Physique Coll.,* **48**(C-1), C1–115-C1-119..
Petrenko, V.F. & Whitworth, R.W., 1999. *Physics of Ice,* Oxford University Press, Oxford.
Petrenko, V.F., 1993. Electrical Properties of Ice, Special Report 93-20, US Army Corps of Engineers, 81pp.
Piolat, L., Revil, A., Cosme, P., Géraud, Y., Dupaigne, T., Wheeler, W., Tveranger, J., Lønøy, B., Turinimana, E., Karangwa, E. & Favier, A., . , , , . https://doi.org/10.1093/gji/ggaf307.
Piolat, L. *et al.* 2025a. Induced polarization of volcanic rocks. 8. The case of intrusive igneous rocks, *Geophys. J. Int.,* **241,** 1348–1372.
Piolat, L. *et al.* 2025b. Induced polarization of volcanic rocks. 9. Anatomy of a rising thermal plume, *Geophys. J. Int.,* **243,** 1.
Ravanel, L., Allignol, F., Deline, P., Gruber, S. & Ravello, M., 2010. Rock falls in the Mont Blanc massif in 2007 and 2008, *Landslides,* **7**(4), 493–501..
Revil, A. & Glover, P.W.J., 1997. Theory of ionic surface electrical conduction in porous media, *Phys. Rev. B,* **55**(3), 1757–1773.
Revil, A. *et al.* 2017a. Complex conductivity of soils, *Water Resour. Res.,* **53**(8), 7121–7147.
Revil, A., *et al.* 2025. Induced polarization as a tool to characterize permafrost. 2. Applications to low and high-porosity environments, Geophys. J. Int.
Revil, A., 2012. Spectral induced polarization of shaly sands: influence of the electrical double layer, *Water Resour. Res.,* **48,** W02517.
Revil, A., 2013. On charge accumulations in heterogeneous porous materials under the influence of an electrical field, *Geophysics,* **78**(4), D271–D291.
Revil, A., Abdel Aal, G.Z., Atekwana, E.A., Mao, D. & Florsch, N., 2015b. Induced polarization response of porous media with metallic particles—Part 2. Comparison with a broad database of experimental data, *Geophysics,* **80**(5), D539–D552., 2015.
Revil, A., Florsch, N. & Mao, D., 2015a. Induced polarization response of porous media with metallic particles—Part 1: a theory for disseminated semiconductors, *Geophysics,* **80**(5), D525–D538..
Revil, A., Le Breton, M., Niu, Q., Wallin, E., Haskins, E. & Thomas, D.M., 2017b. Induced polarization of volcanic rocks. 1. Surface *versus* quadrature conductivity, *Geophys. J. Int.,* **208,** 826–844.
Revil, A., Le Breton, M., Niu, Q., Wallin, E., Haskins, E. & Thomas, D.M., 2017c. Induced polarization of volcanic rocks. 2. Influence of pore size and permeability, *Geophys. J. Int.,* **208,** 814–825..
Scandroglio, R., Draebing, D., Offer, M. & Krautblatter, M., 2021. 4D quantification of alpine permafrost degradation in steep rock walls using a laboratory–calibrated electrical resistivity tomography approach, *Near Surf. Geophys.*, **19,** 241–260..
Shuey, R.T., 1975, *Semiconducting Ore Minerals,* Elsevier publishing Co.
Sillars, R.W., 1937. The properties of a dielectric containing semiconducting particles of various shapes, *J. Inst. Electr. Eng.,* **80,** 378–394.

Stillman, D.E., MacGregor, J.A. & Grimm, R.E., 2013, The role of acids in electrical conduction through ice, *J. Geophys. Res.: Earth Surf.,* **118,** 1–16.

Titov, K., Komarov, V., Tarasov, V. & Levitski, A., 2002. Theoretical and experimental study of time domain-induced polarization in water-saturated sands, *J. App. Geophys.,* **50,** 417–433.

Vinegar, H.J. & Waxman, M.H., 1984. Induced polarization of shaly sands, *Geophysics,* **49,** 1267–1287.

Wan, X., Liu, E., Qiu, E., Qu, M., Zhao, X. & Nkiegaing, F., 2020. Study on phase changes of ice and salt in saline soils, *Cold Reg. Sci. Technol.,* **172,** 102 988.

Waxman, M.H. & Smits, L., 1968, Electrical conductivities in oil-bearing shaly sands, *Soc. Pet. Eng. J.,* **8**(02), 107–122.

Weller, A., Slater, L. & Nordsiek, S., 2013. On the relationship between induced polarization and surface conductivity: implications for petrophysical interpretation of electrical measurements, *Geophysics,* **78,** D315–D325.

Zimmermann, E., Kemna, A., Berwix, J., Glaas, W., Münch, H.M. & Huisman, J.A., 2008. A high-accuracy impedance spectrometer for measuring sediments with low polarizability, *Meas. Sci. Tech.,* **19**(10), 105603.

Zorin, N. & Ageev, D., 2017. Electrical properties of two-component mixtures and their application to high-frequency IP exploration of permafrost, *Near Surf. Geophys.,* **15,** 603–613.